WINDOWS XP: EXPLOITING THROUGH LINUX

Akshit Chauhan[1], Deepak Chandel[2]
[1, 2] Computer Science Department, DCE, GGN, (India)

ABSTRACT

An operating system is a program that manages the computer hardware. It also provides a basis for application program and acts as an inter-mediatory between the user of a computer and the computer hardware. An amazing aspect of a operating system is how varied they are in accomplishing these tasks. Mainframe operating systems are designed primarily to optimize utilization of hardware. Personal computer (PC) operating systems support complex games, business applications and everything in between . Handheld computer operating systems are designed to provide an environment in which a user can easily interface with the computer to execute programs. Thus , some operating systems are designed to be convenient , others to be efficient and others some combination of two. The Microsoft windows XP operating systems is a 32/64-bit preemptive multitasking operating systems for AMD K6/K7, Intel IA32/IA64 and later micro-processors. The successors to Windows XP are also intended to replace the windows 95/98 operating systems. Linux is another operating system , another UNIX-like system That has gained popularity in recent years. It has been designed to run as many standard UNIX applications as possible.

Keywords: Mainframe, Handheld, Multitasking, Linux, Unix, Windows XP.

I. INTRODUCTION

An Operating System is an important part of almost every computer system. A computer system can be roughly divided into four components: the hardware, the operating system, the application programs and the users. The hardware - the central processing unit (CPU) , the memory and the input/output devices – provides the basic computing resources. The application programs such as word processors, spreadsheets, compliers and web browsers define the way in which these resources are used to solve the computing problems of the users. Windows XP is a multi-user operating system , supporting simultaneous access through distributed services or through multiple instances of the graphical user interface (GUI) via the windows terminal server. The server versions of Windows XP support simultaneous terminal server sessions from Windows desktop systems. Windows XP was the first version of windows to ship a 64-bit version. The native NT file system (NTFS) and many of the win32 APIs have always used 64-bit integers where appropriate – so the major extension to 64 –bit in Windows XP is support of large addresses. Windows XP received generally positive reviews with critics noting increased performance (especially in comparison to Windows ME), a more intuitive user interface, improved hardware support, and its expanded multimedia capabilities. Windows XP remained popular even after the release of newer versions, particularly due to the poorly received release of its successor Windows Vista. Vista's 2009 successor, Windows 7, would overtake XP in total market share by the end of 2011. Sales of

Windows XP licenses to original equipment manufacturers (OEMs) ceased on June 30, 2008, but continued for netbooks until October 2010.[1]

The first Linux kernel released to the public was Version 0.01 , dated May 14,1991. It had no networking , ran on only 80836 compatible Intel processors and PC hardware and had extremely limited device driver report. The virtual memory subsystem was also fairly basic and included no support for memory mapped files; however this early incarnation supported share pages with copy-on-write.

Linux was originally developed as a free operating system for Intel x86-based personal computers. It has since been ported to more computer hardware platforms than any other operating system. Linux also runs on embedded systems, which are devices whose operating system is typically built into the firmware and is highly tailored to the system; this includes mobile phones, tablet computers, network routers, facility automation controls, televisions[24][25] and video game consoles.[2]

II. HISTORY OF WINOWS XP AND LINUX

In the mid 1980's, Microsoft and IBM cooperated to develop the OS/2 operating system, which was written in assembly language for single processor Intel 80826 systems. In 1988, Microsoft decided to make a fresh start and to develop a "new technology" (or NT) portable operating system that supported both the OS/2 and POSIX application–programming interfaces (API's). In October 2001 Windows XP was released as both an update to the windows 2000 desktop operating systems and a replacement to windows 95/98. In 2002, the server versions of Windows XP will be available. Windows XP updates the graphical user interface with a visual design that take advantage of a more recent hardware advances and many new ease-of-new features. Microsoft's design goals for Windows XP include security, reliability, windows and PIOSIX application compatibility. Windows XP security goals required more than just adherence to the design standards that enabled Windows NT4.0 to receive C- 2 Security classification from the U.S government (which signifies a moderate level of protection from defective software and malicious attacks.) Linux looks and feels much like any other UNIX system; indeed, UNIX compatibility has been a major design goal of the Linux project. Linux is much younger than any other UNIX system. It's development began in 1991, when a Finnish student Linus Torvalds, wrote and christened Linux, a small but self-contained kernel for the 80386 processor, the first true 32-bit processor in Intel's range of PC-compatible CPU's. In it's early days, Linux development revolve around the central OS kernel – the core , privileged executive that manages all system resources and that interacts directly with the computer hardware. The Linux kernel is entirely original piece of software developed from scratch by Linux community. The Linux system, as we know it today, includes a multiple of components.

III. SOME NECESSARY TERMINOLOGIES

First of all, it is necessary for us to understand some basic terminologies before we actually go on the implementing part.

- **Exploitation** - It is the use of someone or something in an unjust or cruel manner, or generally as a means to one's ends. Here we talk about exploitation of Windows XP.
- **Exploits** - An exploit is a piece of software, a chunk of data, or a sequence of commands that takes advantage of a bug, glitch or vulnerability in order to cause unintended or unanticipated behavior to occur

on computer software, hardware, or something electronic (usually computerized). Such behavior frequently includes things like gaining control of a computer system, allowing privilege escalation, or a denial-of-service attack[3]. The exploit for windows XP is” windows/smb/ms08_067_netap”.

- **Metasploit** – It is one of the tools available in Linux that provides information regarding security vulnerabilities and aids penetration testing and IDS signature development. Metasploit Framework, a tool for developing and executing exploit code against a remote target machine. Other important sub-projects include the Opcode Database, shell code archive and related research.
- **Payloads_-** Metasploit contains many different types of payloads, each serving a unique role within the framework. One of the payload for exploiting Windows XP is “Meterpreter”, the short form of Meta-Interpreter is an advanced, multi-faceted payload that operates via dll injection. The Meterpreter resides completely in the memory of the remote host and leaves no traces on the hard drive, making it very difficult to detect with conventional forensic techniques. Scripts and plugins can be loaded and unloaded dynamically as required and Meterpreter development is very strong and constantly evolving.
- **Shellcode** - This is a set of instructions used as a payload when the exploitation occurs. Shellcode is typically written in assembly language, but not necessarily always. It's called "shellcode" because a command shell or other command console is provided to the attacker that can be used to execute commands on the victim's machine.
- **Module -** A module is a piece of software that can be used by the Metasploit Framework. These modules are interchangeable and give Metasploit its unique power. These modules might be exploit modules or auxiliary modules.
- **Listener -** This is that component that listens for the connection from the hacker's system to the target system. The listener simply handles the connection between these systems.
- **Show -** Metasploit Framework has hundreds of modules and other utilities. As a result, you will not be able to remember them all. Fortunately, the show command can grab a listing of all modules, options, targets, etc. in your framework.

IV. IMPLEMENTATION

- First of all install virtual machine software in your system to test whether out experiment is working or not than we can try at another remote machine.
- Install Kali Linux or Backtrack and windows XP in the virtual machine in order to try our experiment.
- After installing the above two virtual machine’s , we are ready for our experiment.
- Open up the Linux machine in your virtual machine software, as Linux has a command line interface , so open up the terminal window and type “msfconsole” i.e meta-sploit framework console will load up in the terminal window.
- Now apply the following commands one by one
- use exploit/windows/fileformat/ms13_071_theme
- msf exploit (ms13_071_theme)>set payload windows/meterpreter/reverse_tcp
- msf exploit (ms13_071_theme)>set lhost 192.168.223.133
  (IP of your Kali machine to know type ifconfig on new terminal)
- msf exploit (ms13_071_theme)>set srvhost 192.168.223.133

- msf exploit (ms13_071_theme)>exploit

Once all this done you need to give to your victim

\\192.168.1.3:gCzJXDKtJugDsVFC.scr via chat or email or any social engineering technique you can use.

Once the victim open the url provided by you he will asked for confirmation of opening link .

as soon as victim click run you will have your meterpreter shell open

Now you have access to the victims PC. Use "**sessions -l**" and the Session number to connect to the session. And Now Type "**sessions -i ID**

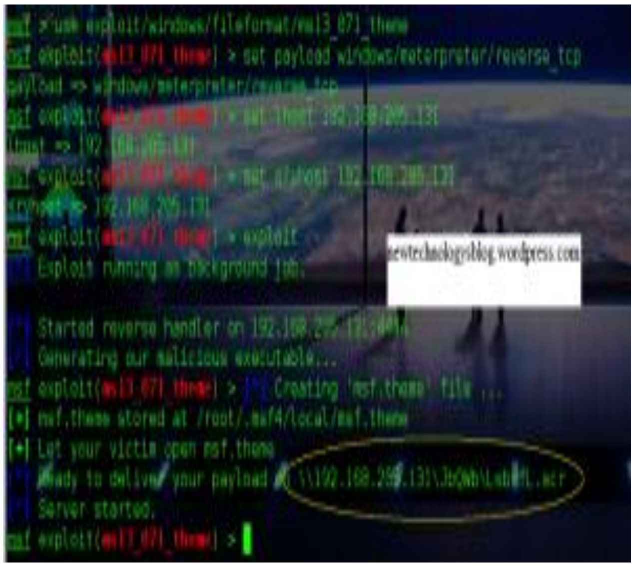

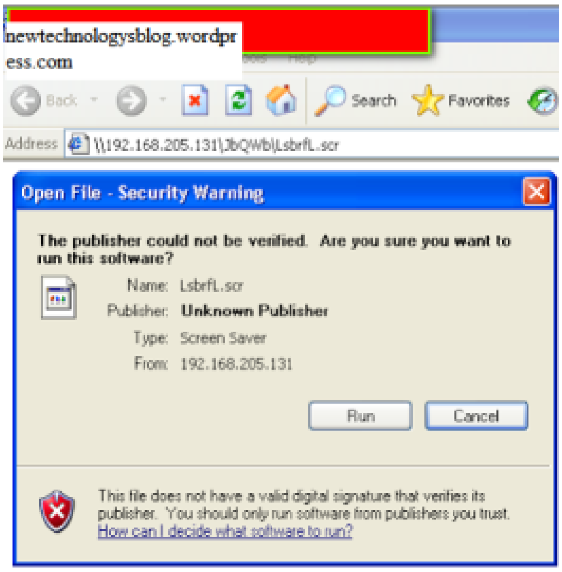

VI. FUTURE SUGGESTIONS

Windows XP is an Operating system with many bugs and vulnerabilities. Therefore Microsoft Inc. has stopped providing support for Windows XP from now on.

Windows 7 (home and basic) , Windows 8 , windows 8.1 are the successful successors of XP.

It's very difficult to hack or penetrate into windows 8 or 8.1 as they come with more embedded security. As Microsoft increases more and more security in their o/s , hacker will use more and more different ways to hack into them. It is impossible to create a software or a o/s without a bug

VII. CONCLUSION

Windows XP and Kali Linux are both o/s but the fact lies that windows Xp is not a secure o/s. As we saw that , by writing some commands and just creating a sessions between two computer's we can actually hack into a windows machine. Therefore one should never ever turn off his/her windows firewall off. The gateway to hack into a remote machine is provided by windows firewall if it's turned off. Applying antiviruses is also a option but to a some extent , not all antiviruses can safeguard your machine.

REFERENCES

[1] Windows XP (Internet Sources: Wikipedia)
[2] Linux (Internet Sources: Wikipedia)
[3] Exploits (Internet Sources: Wikipedia)
[4] http://newtechnologysblog.wordpress.com/2014/04/25/hack-window-xp-with-kali-linux/
[5] www.windows.microsoft.com
[6] www.linux.com
[7] http://www.googlescholar.com
[8] www.Wikipedia.com

EFFECT OF INTERFERENCE AND SHEET-LIKE FAULT SCATTERINGS IN MEASURING CONDUCTIVITY OF $YBa_2Cu_3O_7$ SUPERCONDUCTORS

Dr Rakesh Mohan Bhatt
Dept. of Computer Science & Engineering, HNB Garhwal University, Srinagar Uttrakhand, (India)

ABSTACT

Due to the wide range of applications of superconducting systems in the areas of communication, memory devices etc., thermal conduction estimation has been a great interest of the researchers. The present paper is an attempt to measure the conductivity aiming to observe the effect of different scattering strengths involve during the conduction. The thermal conductivity of $YBa_2Cu_3O_7$ superconductors has been evaluated in the temperature range of 10K to 240K, using computer-based simulation approach considering various scattering strengths due to boundary scattering, point defect scattering, sheet like fault, electron-phonon scattering, interference scattering between point defect and three phonon processes and three phonon U-scattering respectively. These scattering strengths are symbolically referred as A, α, β, γ, δ and $\in$ respectively. With the applications of simulation, in the present paper the effect of scattering strengths of disloction and sheet-like fault in measuring the conductivity of $YBa_2Cu_3O_7$ superconductors is observed. Some interesting results have been observed which dipicts the behaviour of these scattering strenths at different temeratures. For example when interference scattering (δ) and sheet like fault (β) are changed, conductivity values varies from significantly.

Keywords: Scattering, Thermal Conductivity, $YBa_2Cu_3O_7$ Superconductors

I. INTRODUCTION

Research investigations in the field of high temperature superconductors have been carried by several workers due to its peculiar and inherent properties. This has led to its wide theoretical and experimental investigations for the industrial applications[1]. For high temperature superconductors, transport properties have been reviewed by Jezowski and Klamut[2]. Some years back, Ravindran et. al.[3] have theoretically interpreted their measurements in terms of Tewordth and Wolkhausan theory[4], neglecting the dislocation scattering which has been taken into account by considering various scattering strengths viz. dislocation scattering, sheet-like faults, interference scattering between point-defects and three-phonon processes and three-phonon U-scattering combined. This shows the good impact on the conductivity calculations considering these scattering strengths; which has been further analyzed by and R. M. Bhatt et. Al.[5]. In the present analysis, conductivity has been estimated in the temperature range from 10 to 240 K in examining the effect of some scattering strengths. In the following sections, analysis, behavior modeling, results, and discussion have been described. Lastly, a conclusion has been drawn.

II. ANALYSIS

For the estimation of the scattering strengths, the thermal conductivity model of Callaway's[6] is given by [2,4,7] has been taken as follows :

$$K = A\, t^3 \int x4\, e^x / [(e^x -1)^2 . F(t, x)]\, dx \qquad (1)$$

Where F(t,x) is -

$$F(t,x)=[1+\alpha x^4t^4+\beta x^2t^2+ \gamma txg(x,y)+ \delta x^3t^4+ \in x^2t^5] \qquad (2)$$

Parameters A, α, β, γ, δ and $\in$ used in the above equations are referred as the scattering strengths due to boundary scattering, point defect scattering, sheet like fault, electron-phonon scattering, interference scattering between point defect and three phonon processes and three phonon U-scattering respectively. x (= ђ/KT) is the reduced energy, T (= T/T_c) is the reduced temperature and g(x,y) is the BRT function, defined by Bardeen et.al.[8].

In the present analysis, some interesting results have been observed which depicts the behavior of these scattering strengths at different temperatures. Following section discussed the result so obtained.

III. RESULT

The thermal conductivity of $Yba_2Cu_3O_7$ superconductors has been evaluated using Eq.-1 and Eq.-2 in the temperature range of 10K to 150K, using computer-based simulation approach for A, α, β, γ, δ and $\in$ the scattering strengths. Keeping the above mentioned approach for the behavior modeling, thermal conductivity has been measured in the temperature range from 10K to 150K by assigning different values to the scattering parameters. These estimated results are compared with the experimental results and found a good match with the experimental results of Ravindran et. al.[3]. The various parameters used in the present analyses are mentioned in the Table-I and graphical presentation is in the Fig.-1.

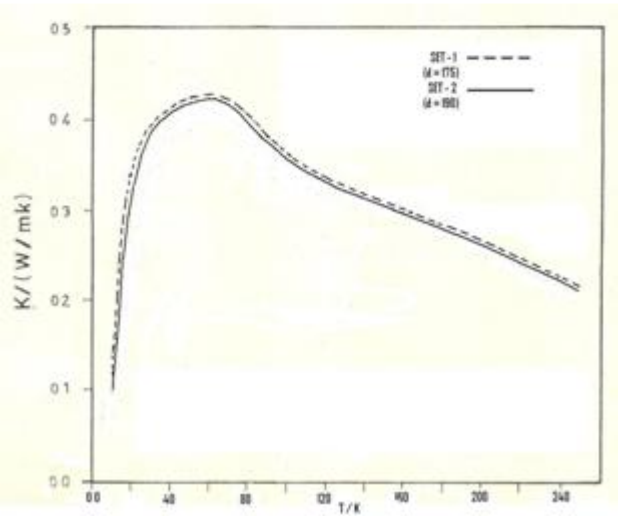

Fig.1. Conductivity of $Yba_2Cu_3O_7$ for SET-1 and SET-2

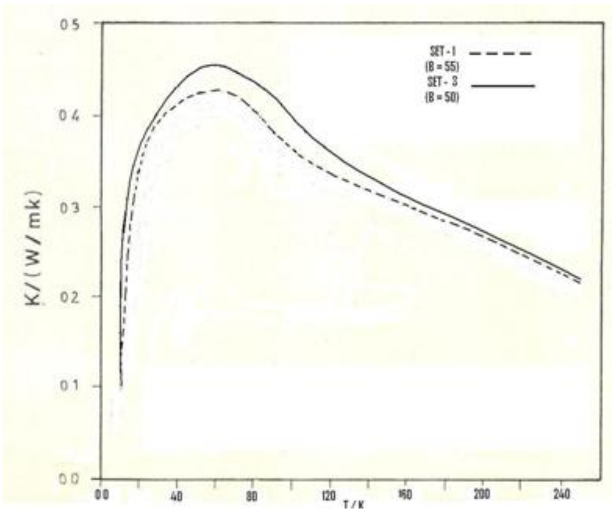

Fig.2. Conductivity of $Yba_2Cu_3O_7$ for SET-1 and SET-3

Further, after validating the conductivity up to 150K with the help of experimental results, the model is simulated over different parameters to examine and predicting the behavior at different levels of temperature. Following Table-1 contains four results viz. Reading-A, B, C, and D corresponding to different values of the scattering strengths. Maximum conductivity so obtained is also shown with the conductivity values in the temperature range of 80K to 240K. Simulation approach[9,10] has been applied in generating different responses for three sets of parameters shown in Table 1and their corresponding conductivity values have been tabulated in the Table -2.

Table-1: Parameters of Scattering Processes

Sr. No.	Parameters					
	A	γ	α	β	∈	δ
Set -1	4.0	25	10	55	.20	175
Set -2	4.0	25	10	55	.20	190
Set -3	4.0	25	10	50	.20	175

Table-2: Conductivity of YBCO Superconductor

Temp/ K	Conductivity ($W\,cm^{-1}K^{-1}$)		
	SET-1	SET-2	SET-3
10	1.3878	1.3785	1.4758
20	2.8622	2.8111	3.0286
30	3.6971	3.5980	3.8799
40	4.1194	3.9818	4.2935
50	4.3121	4.1471	4.4711
60	4.3759	4.1923	4.5200
70	4.3630	4.1667	4.4940
80	4.3015	4.0968	4.4208
90	4.2083	3.9982	4.3168
100	4.0946	3.8814	4.1930
110	3.9685	3.7540	4.0572
120	3.8358	3.6215	3.9154
130	3.7006	3.4877	3.7780
140	3.5661	3.3556	3.6299
150	3.4344	3.2269	3.4912
160	3.3067	3.1029	3.3574
170	3.1839	2.9842	3.2292
180	3.0666	2.8713	3.1070
190	2.9550	2.7641	2.9911
200	2.8489	2.6627	2.8813
210	2.7485	2.5668	2.7775
220	2.6534	2.4763	2.6795
230	2.5634	2.3909	2.5870
240	2.4784	2.3103	2.4996

In examining the effect of interference and sheet-like fault, the above results have been discussed below.

IV. EFFECT OF INTERFERENCE AND SHEET-LIKE FAULT SCATTERINGS

With the applications of simulation, in the present paper the effect of scattering strengths of disloction and sheet-like fault in measuring the conductivity of $YBa_2Cu_3O_7$ superconductors. Some interesting results have been observed which dipicts the behaviour of these scattering strenths at different temeratures e.q. when interference scattering (δ) is 175 then the value of conductivity starts from 0.13785 at 10K and ends with 2.31030 at 240K; further, when interference scattering is increased to 190 then the value of conductivity starts from 0. 13878 at 10K and ends with 2.4784 at 240K. This shows that increase in the interference scattering increases the conductivity. In contrary to this behaviour, when the value of sheet like fault (β) is decreased from 55 to 50, conductivity values varies from 0.13878 to 0.14758 at 10K and from 2.4784 to 2.4996. Shifting of the gradient of the temperatur between 20 to 60K towards left-side can also be observed through its graphically reprented figure.

V. CONCLUSION

Some interesting results have been observed to infer the effect of scattering strengths of interference (δ) and sheet-like fault (β) in measuring the conductivity of $YBa_2Cu_3O_7$ superconductors to dipict the behaviour of these scattering strenths at different temeratures. Further, it can be concluded that this kind of pre-experimental test helps in saving the resources involved.

VI. ACKNOWLEDGEMENT

Computational facilities availed at the Deptt. of Computer Science & Engineering, HNB Garhwal University is sincerely acknowledged. Fruitful discussion with Prof. R. P. Gairola of Physics department, HNB Garhwal University, Srinagar, Uttrakhand, India is also sincerely acknowledged.

REFERENCES

[1] Hyo-Sang Choi, Ok-Bae, Hye-Rim Kim, and Kwon-Bae Park,Switching Properties of a Hybrid Type Superconducting Fault Current Limiter Using YBCO strips, IEEE transaction on applied superconductivity,14(3), 2002, 1833-1837.

[2] A. Jezowski, *Phys. Lett. A*, 122, 1987, 431.

[3] T. R Ravindran, V. Sankaranarayana, and R.Srinivasan , *Pramana-J.Physics*, 32, 1992, 109.

[4] L. Tewordt and Th. Wolkhausan, *Solid State Commun*., 70, 1989, 839.

[5] R. M. Bhatt, and R. P. Gairola, *Simulation analysis of the YBCO superconductors*, publicshed in the Journal- Current Science, Bangalore,80(7), 2001, 864-867.

[6] J. Callaway, *Phys.Rev.*,113, 1959, 1046.

[7] R.P. Gairola, *Phys. St. Sol. (b)* 125, 1985, 65.

[9] Avril M Law, *Simulation modeling and analysis* (Tata McGraw Hill, 2008).

[8] J. Bardfeen, G. Rickayzen and L. .Tewordt, *Phys. Rev.*, 132, 1963, 2461.

[10] Gordon Jeoffery, *System simulation* (PHI, 2008).

MODEL OF PHONON CONDUCTIVITY FOR MAGNESIUM STANNIDE

Dr Rakesh Mohan Bhatt

Dept Computer Science & Engg. Hnb Garhwal University, Srinagar, Uttrakhand, (India)

ABSTRACT

Due to its peculiar properties, the non metallic solids have been important elements in the semiconductor device industry. Particularly, the estimation of phonon conductivity of such solids becomes important for their applications. Magnesium Stannide (Mg_2Sn) is one of the such elements in the present study to analyses the phonon conductivity. In the presence of the interaction term which dominants near the low temperature and the exponential temperature dependence which dominants significantly at the higher temperature. In the estimation of the phonon conductivity, the inter-dependence of the relaxation rates, due to isotopic impurities ($\tau^{-1}_D \sim A\omega^4$) and anharmonic interactions ($\tau^{-1}_A = B\omega^2T^3$) has been considered in the form of a cross term (Γ^{AD}). The present study investigates the role of the cross term (in explaining the low temperature lattice thermal conductivity, of solids, doped with isotopic impurities) and the exponential temperature dependence of the parameter (due to its significant role at high temperature) have been analyzed using the model on the computer. A good agreement has been achieved with experimental data nearly up to 70K which validates the model computed on computer.

Keywords: Computer Applications, Model, Magnesium Stannide, Phonon Conductivity

I. INTRODUCTION

The non metallic solids have been important elements in the semiconductor device industry. Particularly, the estimation of phonon conductivity of such solids becomes important for their applications. Magnesium Stannide (Mg_2Sn) is one of the such elements which has been analyzed in the present study by measuring is conductivity. Doped with isotopic impurities, the estimation of phonon conductivity of non metallic solids has been an important application area in the semiconductor device industry. Because of their wide applications, measuring of thermal conductivity of these solids has been a great interest among the researchers[1-4]. The present work analyses the thermal conductivity of intrinsic semiconductor, of which the transport behavior is similar to the insulator with heat conduction due to lattice waves i.e. phonons. The present study does not consider the electronic contribution in the thermal conductivity measurement. The model given by Callaway[5] has been used to by above mentioned researchers particularly for the low temperature range. In the measurement of phonon conductivity, they have directly assumed that the relaxation rates due to isotopic impurities ($r^{-1}_D \sim A\omega^4$) and anharmonic ($r^{-1}_A = B\omega^2T^3$) are independent of each other, which are then added in accordance with Mathiessen's rule and that there is no interference or cross term of defect with anharmonic parameters, appearing in the total phonon relaxation time. in estimating the thermal conductivity of doped crystals, this cross term (r^{AD}) cannot be ignored in the exact calculations, particularly near the low temperature maximum , where the conventional domination of r^{-1}_D ends and that of r^{-1}_A starts. The present paper investigates the role of this cross term, in explaining the low temperature lattice thermal conductivity, of solids, doped with isotopic impurities. In addition, exponential temperature dependence of the parameter B_2 as discussed below has also been taken into account due to its significant role at high temperature as proposed by Gairola[6]. For conduction calculations, computer aided simulation approach has already been in use e.g. Osetsky[7] has applied simulation to study the high temperature phase stability in iron, a good conductor. The proposed model is also simulated with modified steps by Bhatt and Gairola[2] in the preliminary work on semiconductors taking account the basic method mentioned by Gordon [8] and Avil[9]. The following sections discuss the phonon conductivity model, results, analysis and lastly the conclusion.

II. PHONON CONDUCTIVITY MODEL

In analyzing the phonon conductivity of Mg_2Sn, as measured earlier by Martin and Danielson[10] up to 50^0K, the present estimation is done in the temperature range 4 – 82^0K, using the simulation approach, as described by Bhatt and Gairola[9] to achieve consistency with the experimental results. It has been a usual practice, to generally neglect the exponential temperature dependence of the parameter B_2, representing Umklapp phonon-scattering and both B_1 (normal phonon scattering parameter) and B_2 are lumped into single parameter B, assumed to be independent of T, as considered earlier by Bhatt and Gairola[11] for the analysis of Ge. This is because, at low temperature B_2 does not change significantly with T but at higher temperature it changes considerably. Therefore, B_2 is taken to depend upon T, exponentially, as has also been considered by Martin and Danielson[10], in analyzing conductivity of Mg2Sn. Their theoretically analyzed curve, however, shows poor agreement above 50^0K. In the present study, the effect of the change in B1 has also been analyzed. In the following sub-sections, modeling and simulation has been discussed.

2.1. Modeling

As the present analysis is rigorous and involves less approximation in comparison to other models, therefore, simulation techniques has been applied on the mathematical model as proposed by Gairola[12] which a modified version of Callaway's model[5] and being iteratively computed. The following equation shows the mathematical/computational model taken for the simulation process :

$$\tau^{-1} = v/FL + A\omega^4 + [B_1+B_2 \exp.(- \Theta/aT)]\, \omega^2 T^3 + D\, \omega^3 T \qquad \ldots(1)$$

This mathematical model as shown by the Eq.-1 above, has been computed for the estimation of phonon conductivity of Mg_2Sn in the temperature range 4 – 90 K considering the previous approach [9]. In this Computation, out of several responses, only relevant response has been considered which shows similar experimental values.

2.2. Simulation

There are five stages[9] which are selectively mapped-out for computer-based simulation process viz. entities/attributes & activities; system image & routine; simulation procedure; report generation & storing; and interaction interface. In the last phase, the flow of simulation process is being interacted by assigning new values of parameters/attributes in the model so as to find the experimental results[14]. So in achieving such useful simulated responses, arithmetic and logical conditions have been applied and manipulated to decide to accepted or neglected the simulated responses. These responses have been discussed in the following section.

III. RESULT

On the basis of above defined methodology, the model is being simulated and suitable responses have been gathered as shown in the Table-1 and Table-2. Nine parameters have been assigned the values as shown in the Table-1.

Table-1: Parameters

Parameters	Values
v	359 cm/sec
L	.11
F	.54
α	2.5
Θ_D	154
A	6.3×10^{-44} sec^3
B_1	7.7×10^{-23} sec K^{-3}
B_1	4.7×10^{-23} sec K^{-3}
D	2.75×10^{-33} sec^3 K^{-1}

Using these values of nine parameters, phonon conductivity has been measured at 14 different stages of the temperature in the range of 4 – 90^0K. Following Table-2 shows the corresponding to the results for the conductivity for each stage of the temperature taken.

Table-2: Phonon Conductivity

Temperature (Kelvin)	4	6	8	10	14
Conductivity ($Wcm^{-1}K^{-1}$) x 10^7	0.9672	2.374	3.878	5.125	6.296
Temperature (Kelvin)	20	26	30	36	40
Conductivity ($Wcm^{-1}K^{-1}$) x 10^7	5.322	3.592	2.710	1.818	1.425
Temperature (Kelvin)	50	60	70	82	90
Conductivity ($Wcm^{-1}K^{-1}$) x 10^7	0.837	0.539	0.372	0.255	0.2050

The results of the Table-2 have been graphically represented in the Fig.-1; where experimental points have been marked as circles and the present study with the solid line. In the present investigation, the role of the cross term (in explaining the low temperature lattice thermal conductivity, of solids, doped with isotopic impurities) and the exponential temperature dependence of the parameter B_2 (due to its significant role at high temperature) have been analyzed.

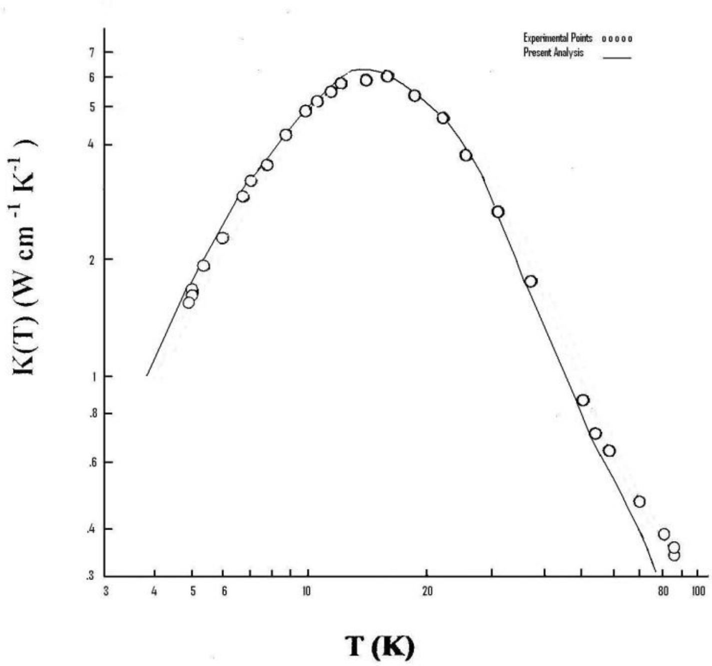

Fig.-1: Phonon Conductivity Of Mg_2Sn

It is evident from the Fig.-1, that a good agreement has been achieved with experimental data up to 60°K. This validates the role of these terms in the proposed model. Further, the simulation process also optimizes the approach of the conductivity estimation. Further, it has also been observed from the previous work[16] that by decreasing the B1 parameter from 7.7 to 7.0 in the present case, at lower and higher temperature ranges that up to 20K and above 30K onwards no any much deviation in the conductivity values have been noticed but a significant variations have been observed in the mid temperature range i.e. from 20 to 30K.

V. CONCLUSION

The present study concludes that the existence of the interaction term dominants near the low temperature and the exponential temperature dependence which dominants significantly at the higher temperature; which is apparently depicts from the result and the figure. On comparing these results, significant observations are being notices near the mid range of temperature.

ACKNOWLEDGMENT

The computing facilities received at the Deptt. of Computer Science and Engineering, HNB Garhwal University is sincerely acknowledged. Fruitful discussion with Dr R P Gairola is also sincerely acknowledged.

REFERENCE

[1] P. Carruthers, *Rev.Mod.Phys*., 33, 1961, 92.

[2] P. G. Klemens P.G., *Solid state physics* (Academic Press, New York ,1958).

[3] J. J. Martin , Thermal Conducticity of Magnesium Stannide *J. Phys. Chem. Solids* 33, 1972, 1139.

[4] Varujan Kevorkijan and Sreco Davorkapin, Preparation and study of Mg2Sn-based composites with different compositions, Material and Technology, 44(5), 2010, 251-259.

[5] Joseph Callaway, *Phys. Rev.* 113, 1959, 1046.

[6] R. P. Gairola, Low-Temperature Lattice Thermal Conductivity of Nonmetallic Solids with Isotopic Impurities, *Phys.stat.sol.(b)*, 125, 1984, 65.

[7] Osetsky Yu N., Computer-simulation study of high temperature phase stability in iron, *Phys. Rev. B*, 57(2), 1998, 755-763.

[8] Gordan Geoffrey, System simulation (Prentice-Hall of India, AIE Transactions, 3, 2008).

[9] R. M. Bhatt, and R. P. Gairola, Foundation for Virtual Experimentation to evaluate thermal conductivity of Semi and Superconducting materials, *AI in theory & practice II*, (Max Bramer : Springer, 2008).

[10] J. J. Martin and G. C. Danielson, *Phys. Rev.* 166, 1968, 879.

[11] R. M. Bhatt and R. P. Gairola, Simulation Analysis of Phonon Conductivity of Germanium, Proc. Annual Convention of Computer Society of India, Bangalore, India, 2002, 121-124.

[12] R. P. Gairola, *Acta phys. Polon.*, A63, 1983, 121.

[13] R. M. Bhatt, Phonon Conductivity Estimation Model for Magnesium Stannide, Proc International Conf. on Advanced Modeling, Optimization & Computers, Roorkee, 343-347.

[14] Avril M Law, *Simulation modeling and analysis* (Tata McGraw Hill, 2008).

ADAPTIVE BIT INTERLEAVED CODED MODULATION FOR MOBILE RADIO OFDM SYSTEMS BY USING RICIAN FADING CHANNEL

[1]Ramasiva Shankar T.M, [2]Aruna Kumari S
[1]*Department of ECE, Malla Reddy College of Engineering& Technology, Hyderabad, (India)*
[2]*Department of ECE, Malla Reddy College of Engineering& Technology, Hyderabad, (India)*

ABSTRACT

NOW a day's industries require some special techniques due to increase in wireless communications. These techniques should solve the communication related problems and challenges and improves the quality of service. When the signal propagates from transmitter to receiver it undergoes to some random fluctuations called Noise. This will happened in both time and frequency domain. We need to predict such noise and eliminate it. The need of predicting noise and measure of it is referred as Channel state information simply CSI. This is the measurement of noise prediction. But, here the measurement will be observed after some time units. The transmitter selects appropriate modulation technique depending on the Channel state information. This process is called as Adoption. In this process transmitter and receiver both need to send acknowledgement to each other to confirm whether it received or not. This method is referred as Channel state information feedback. These techniques combined together is referred as the adaptive bit interleaved coded modulation simply ABICM. There are so many other techniques are there like UAM, ATCM and BICM. Previous method called BICM was based on Bhattacharya bound. This method was works based on minimum distance of constellation and a nominal non-adaptive BICM. It works by determine the Constellation size and transmission power. ATCM method or adaptive trellis coded modulation gives better performance but outdated. So, Proposing ABICM was based on expurgation bounded aided by fading prediction. This ABICM method improves the accuracy of bit error rate (BER). This method also gives better spectral efficiency and performance.

Keywords: Adaptive Modulation, Fading Channels, Interleaved Coding, Frequency Division Multiplexing And Resource Management.

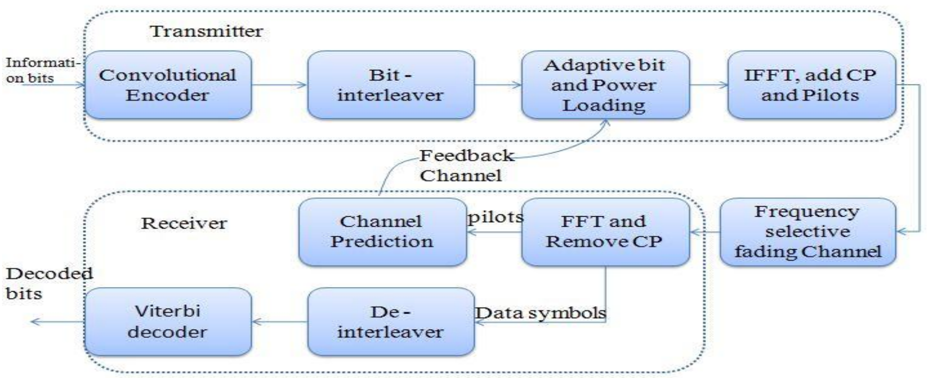

Fig.1 System diagram of LRP-enabled adaptive OFDM system with ABICM using Rician Channel.

I. INTRODUCTION

THE adaptive bit-interleaved coded modulation (ABICM) was projected in [1] to enhance lustiness of adaptive coded modulation to unreliable channel state info (CSI). Within the original ABICM technique [1], the Bhattacharyya certain supported the minimum distance of the constellation and a nominal non-adaptive BICM theme were utilized to work out the constellation size and therefore the transmission power. The particular BER of this technique significantly deviates from the specified target BER [1], [2]. Hence, extra experimental energy adaptation is needed to keep up the BER. ABICM was additionally investigated in [3], [4] below the idea of excellent CSI at the transmitter, that is affordable for static attenuation channels like indoor wireless systems, however not for out of doors mobile radio channels. Moreover, because of the issue of evaluating the precise BER, simulations were utilized in [3], [4] to get the thresholds that confirm the transmission constellation similarly as power. The censored certain provide correct BER estimates for non-adaptive BICM in additive white mathematician noise (AWGN) and attenuation channels [5]. Rician fading is a stochastic model for radio propagation anomaly caused by partial cancellation of a radio signal by itself — the signal arrives at the receiver by several different paths (hence exhibiting multipath interference), and at least one of the paths, typically a line of sight signal, is much stronger than the others. In Rician fading, the amplitude gain is characterized by a Rician distribution. A Rician fading channel can be described by two parameters: K and Ω. K is the ratio between the power in the direct path and the power in the other, scattered, paths. Ωis the total power from both paths ($\Omega=V^2+2\sigma^2$), and acts as a scaling factor to the distribution. The received signal amplitude (not the received signal power) R is then Rice distributed with parameters

$$v^2 = \frac{K\ \Omega}{(K+1)}$$

And $\sigma^2 = \frac{\Omega}{2(K+1)}$

The resulting PDF then is:

$$f(x) = \frac{2(K+1)x}{\Omega} \, exp\left(-K - \frac{(K+1)x^2}{\Omega}\right) I_o\left(2\sqrt{\frac{K(K+1)x}{\Omega}}\right)$$

Where $I_o(0)$ the 0th order is modified Bessel function of the first kind.

During this letter we have a tendency to style associate degree ABICM system power-assisted by imperfect CSI by using the censored certain. The power to keep up the target BER exploitation this technique is incontestable exploitation simulations for associate degree adaptive orthogonal frequency division-multiplex (OFDM) system. In [1] the performance of ABICM was evaluated exploitation the CSI sample calculable at the receiver and fed back to the transmitter. Because of speedy attenuation variation, this CSI becomes noncurrent, and attenuation prediction is important to keep up re-liable performance [6], [7]. during this letter, we have a tendency to use associate degree autoregressive model-based four-dimensional long vary attenuation predictor (LRP) technique [6] for associate degree OFDM system in numerical comparisons of ABICM, uncoded adaptive modulation, and adaptive trellis coded modulation (ATCM) [8].In this comparison, we have a tendency to show the prevalence of ABICM for sensible mobile radio systems with feedback delays.

In Section II, the adaptive OFDM channel model, the prediction method, and the bit and power loading algorithm are summarized. Section III discusses the original method in [1] and our ABICM method based on the expurgated bound. Numerical results are presented in Section IV, and conclusions are contained in Section V.

II. ADAPTIVE OFDM AIDED BY LONG-RANG EPREDICTION

II. (i) Channel Model and Long-Range Prediction

The system of block diagram of the adaptive OFDM system under investigation is shown in Fig.1. We tend to assume the frequency-selective wide-sense stationary (WSS) Rician fading channel as in [1]. The received signal for the l^{th} subcarrier (l=1…..L) of the n^{th} OFDM symbol is

$$Y(n,l)=H(n,l)X(n,l)+W(n,l) \qquad (1)$$

Where H(n,l) are the complex Gaussian channel response $H(n,l) \sim CN\ (0,1)$, the transmitted signal, and the complex additive white Gaussian noise with variance N_0, respectively. It is assumed the inter-symbol interference (ISI) is removed using appropriate cyclic prefix. Without loss of generality, we set $H\ (n,l) = E_p$ for pilot symbols, where E_p is the pilot symbol energy. To facilitate the LRP, pilot symbols are inserted in both frequency and time domains. Past pilot observations with in a rectangular area that includes $[2p_f+1]$ pilot tones and P_t past pilot OFDM symbols are employed to predict the current channel coefficient H (n,l) [2,Fig.4.2]. In this letter, we assume that channel statistics are known and construct a linear minimum mean square error (MMSE) predictor of order $(2p_f+1)\ p_t$ [2]. In practice, similar prediction accuracy can be achieved by the auto-regressive (AR) model based predictors that track fading channel variations. The performance of this predictor can be improved at low and medium SNR by employing noise reduction [2], [9], [10]. However, we do not utilize noise reduction since we focus on robustness of adaptive coding methods to imperfect predictions. The channel coefficient H (n,l) and its linear MMSE prediction $H^{\wedge}(n,l)$ are jointly Gaussian distributed [1], [7]. The quality of prediction is usually measured by the prediction MMSE

$$\sigma^2 = E\ [|H(n,l) - \hat{H}(n,l)|^2\ ]$$

Suppose the maximum Doppler frequency of the channel is f_{dm}, and we need to predict τ second ahead of the most recently observed OFDM symbol. Then the corresponding normalized spatial prediction range is, which is usually expressed in the unit of carrier wavelength λ [7].

II. (ii) Adaptive Bit and Power Loading

At the transmitter, the data bits are encoded employing a fixed rate convolution encoder, followed by bit-interleaving (Fig. 1). To facilitate analysis, we tend to assume that this interleaver is good as in [1], [5]. As a result of frequency diversity in OFDM systems, this assumption is realistic even for brief interleaving depth in time. After interleaving, the adaptive bit and loading rule maps the coded bits into M-Quadrature receiver. While not loss of generality, we tend to contemplate the allocation for one OFDM symbol X (n,l). Given foreseen channel coefficient $H^{\wedge}(n,l), l \in [1, L]$, suppose the minimum average image energy needed to transmit mil coded bits/symbol whereas maintaining the target BER is $E_{H^{\wedge}(n,l)}(ml)$. Our objective is to maximize the spectral efficiency below the energy constraint E_T, i.e., amplitude modulation (MQAM) symbols for all subcarriers. The constellation sizes and energies of those symbols are determined exploitation the CSI fed back from the

$$max\{\textstyle\sum_{l=1}^{L} m_l\}\ subject\ to\ \textstyle\sum_{l=1}^{L} E_{\hat{H}(n,l)} \qquad (2)$$

If $E_{H^{\wedge}(n,l)}(ml)$ is Known, the distinct water filling algorithmic rule supported the greedy principle achieves the optimum answer of (2) [11]. However, it's difficult to see the perform $E_{H^{\wedge}(n,l)}(ml)$ for given H^(n,*l*). This downside needs a good analytical estimate of the common BER for every modulation level as a function of the expected CSI. For totally studied un coded adaptive modulation [12] and ATCM [8], the function $E_{H^{\wedge}(n,l)}(ml)$ may be derived from the BER analysis of MQAM and trellis-coded modulation (TCM) in AWGN channel (see, e.g., [13], [14], [15]). However, for ABICM, antecedently projected techniques don't give correct BER estimates as mentioned earlier. Within the following section we have a tendency to review the initial ABICM technique in [1] and propose a unique technique supported the censored sure.

III. ABICM WITH IMPERFECT CSI

III. (i) ABICM technique

In ABICM, the candidate Gray-labeled MQAM constellations are $\{\chi_m\}$of sizes $|\chi_m| = 2m, m \in M,$ wherever M is that the set of attainable bits per image utilized by the adaptive modulator. Let $d_{min,m}$ and E_m denote the minimum Euclidian distance and average symbol energy of constellation χ_m Respectively. The error Probability of choosing the symbol X $\in\chi$m at the receiver when $X \in \chi_m$is transmitted (the single image error probability) is taken into account in [1]. Given the expected channel coefficient $H^{\wedge}$ (n,*l*), the Bhattacharyya sure of this error likelihood is [1], [2]

$$P[X \to \hat{X}|\hat{H}(n,l)] \leq \frac{1+K}{1+K+C} \; exp\left(-\frac{KC}{1+K+C}\right) \qquad (3)$$

Where, K= $|\hat{H}(n,l)|^2/\sigma^2$ and

$C = d^2{}_{min,m}(K+1)\sigma^2/4\,N_0.$

To relate this sure to the target BER, a non-adaptive BICM theme referred to as the nominal theme that uses fixed MQAM modulation, is utilized in [1]. The nominal theme and also the ABICM theme underneath investigation use a similar convolution encoder. For the nominal theme, the SNR needed to realize the target BER is set by simulation, and also the corresponding Bhattacharyya sure on the one image error likelihood is denoted D0 (This sure is computed from (3) by setting $H^{\wedge}$(n,*l*)=0 since the nominal theme isn't adaptive). as an example, a nominal theme that uses QPSK constellation and rate 2/3, 4-state convolution encoder achieves the target BER=$10^{\wedge}5$ at 17.2 dB, and also the ensuing D0 = 0.0367 [1]. it's argued in [1] that the BER of ABICM is maintained just about at the target BER if the Bhattacharyya sure (3) for ABICM is equal to or smaller than D0. Hence, to take care of the target BER, the energy needed to use the constellation for the l^{th} subcarrier is

$$E_{\hat{H}(n,l)}(m_l) = arg\ min_{E_{m_l}} \left\{\frac{1+K}{1+K+C} \; exp\left(-\frac{KC}{1+K+C}\right) \leq D_0\right\} \qquad (4)$$

There are potential problems with this approach, which we refer to as the original ABICM method. First, single symbol error probability is considered in (3), while the performance is usually measured by the BER. Second, the Bhattacharyya bound in (3) is inaccurate. Finally, the utilization of the nominal scheme is not justified, and the guidelines for selecting the nominal scheme are not provided. As a result, the simulated BER can deviate significantly from the target BER, and the actual transmit power has to be adjusted by simulations to meet the desired BER.

III. (ii) ABICM method based on the Expurgated Bound

The expurgated bound proposed in [5] provides an accurate BER estimate for non-adaptive BICM, which does not require the CSI knowledge. We develop a method based on the expurgated bound for ABICM systems with predicted CSI. Suppose the transmitted coded bit sequence and their estimates are c and c^, respectively. These sequences originate and terminate at the same state and differ by d bits. The channel predictions and constellations associated with these d error bits are $\widehat{H} = [\widehat{H}^1 \widehat{H}^2 \widehat{H}^3 \ \ldots\ldots \widehat{H}^d]$ and $X = [X^1 X^2 \ \ldots\ldots .. X^d]$, respectively. For the i[th] error, the constellation size $|X^i| = 2^{m^i}, i \in [1, d]$. Due to the assumption of ideal interleave, the corresponding channel coefficients $H = [H^1 H^2 H^3 \ \ldots\ldots H^d]$ are independent random variables and the conditional probability density function (PDF) is $p(H|\widehat{H}) = p(H^1|\widehat{H}^1) \ldots . p(H^d|\widehat{H}^d)$ Knowledge of $\widehat{H}$ and X, the pair-wise error probability (PEP) is bounded by eq (5)

$$p(\bar{c} \to \hat{c}|\aleph, \widehat{H}) \le f_{ex}(d, \mu, \aleph, \widehat{H}) \cong \frac{1}{2\pi j} \int_{\varepsilon - j\infty}^{\varepsilon + j\infty} \prod_{i=1}^{d} \varphi_{ex}^{i}(s) \frac{ds}{s}, \tag{5}$$

Where μ is the labeling rule, ε is a small
Positive number [16], and

$$\varphi_{ex}^{i}(s) = E\left[e^{-s\Delta(X,\hat{Z})}\right] = \frac{1}{m^i 2^{m^i}} \sum_{p=1}^{m^i} \sum_{c=0}^{1} \sum_{X \epsilon X_{\bar{c},p}^{i}} \varnothing_{\Delta(X,\hat{Z})(s)}^{H^i} \tag{6}$$

From above equation,m^i is the size of constellation χ^i, $X_{\bar{c},p}^i$is the subset of χ^i where the p[th] bit takes on the value, Δ(X, $\hat{Z}$) is the metric difference between two symbols X and $\hat{Z}$,where $\hat{Z}$is the unique nearest neighbor of X in χ^i that satisfies$\hat{Z} \in X_{\bar{c},p}^i$.We use $\bar{c}$ to denote the complement of bit c. Finally, $\varnothing_{\Delta(X,\hat{Z})(s)}^{H^i}$ is the Laplace transform of the PDF of Δ (X ,$\hat{Z}$)

$$\varnothing_{\Delta(X,\hat{Z})}^{H^i} \triangleq E\left[e^{-s\Delta(X,\hat{Z})} \middle| \widehat{H}^i, X, \hat{Z}\right] \tag{7}$$

To calculate$P(X \to \hat{Z}|\widehat{H}^i)$, the maximum likelihood (ML) detection with the knowledge of perfect CSI H^i at the time of detection is assumed. Denote the received symbol as Y. The conditional probability of Y is

$$p_{H^i}(Y|X) = \frac{1}{\pi N_o} \exp\left(-|Y - H^i X|/N_o\right) \tag{8}$$

Then the metric difference between X and $\hat{Z}$ at the decoder is

$$\Delta(X, \hat{Z}) = \log p_{H^i}(Y|X) - p_{H^i}(Y|\hat{Z}) \tag{9}$$

Using$p_{H^i}(Y|X)$ and $\Delta(X, \hat{Z})$ these equations, substitute in $\varnothing_{\Delta(X,\hat{Z})}^{H^i}$ now we can get

$$\varnothing_{\Delta(X,\hat{Z})}^{H^i} \triangleq \frac{exp\left(-\frac{\frac{s(1-sN_o)K|X-Z|^2}{K+1}}{1+\frac{s(1-sN_o)K|X-Z|^2}{K+1}}\right)}{1+\frac{s(1-sN_o)K|X-Z|^2}{K+1}} \tag{10}$$

As stated earlier, for each bit rate m, our goal is to determine the symbol energy that satisfies the target BER given predicted channel coefficient H^. Although the analytical BER needed to achieve this goal can be derived from PEP, the calculation of PEP in (5) requires the knowledge of channel predictions, transmission energies, and constellation sizes for all d errors. Due to random interleaving, this knowledge is not available in practical systems. Therefore, we simplify (5) by assuming $\varphi_{ex}^{i}(s) = \varphi_{ex}^{io}(s)$ for all $i \epsilon [1, d]$where io is one of the d indices with given $H\hat{}i0 = \widehat{H}$ and $\chi_{i0} = \chi_m$. This assumption is justified by the observation that the bit-loading algorithm selects the symbol energy and the constellation to maintain the same performance for all symbols, and $\varphi_{ex}^{io}(s)$ determines the error probability of each symbol. Thus, a simplified expurgated bound on PEP, which employs $\widehat{H}$ and χ_m instead of vectors $\widehat{H}$ and χ, is defined as

$$\hat{f}_{ex}(d,\mu,\aleph_m,\widehat{H}) = \hat{f}_{ex}(d,\mu,\chi^{i_o},\widehat{H}^{io}) \triangleq \frac{1}{2\pi j}\int_{\varepsilon-j\infty}^{\varepsilon+j\infty}[\varphi_{ex}^{io}(s)]^d\frac{ds}{s} \qquad (11)$$

The above equation is exactly the expurgated bound on PEP for non-adaptive BICM that uses constellation χ_{min} the Rician fading channel with K factor $|\widehat{H}|^2/\sigma^2$. It can be solved numerically using the method proposed in [16].

For a rate k_c/n_c convolution encoder with the free Hamming distance d_{free}, the union bound on the BER is

$$p_b \le \frac{1}{k_c}\sum_{d=d_{free}}^{\infty} W_I(d)\,\hat{f}_{ex}(d,\mu,\aleph_m,\widehat{H}) \qquad (12)$$

Where $W_I(d)$ are the weights of the error events at the Hamming distance Using (9), the average symbol energy that satisfies the BER constraint is derived:

$$E_{\widehat{H}(m)} = arg\ \min_{E_m}\left\{\frac{1}{k_c}\sum_{d=d_{free}}^{\infty} W_I(d)\hat{f}_{ex}(d,\mu,\aleph_m,\widehat{H}) \le BER_{tg}\right\} \qquad (13)$$

Where BER_{tg} is the target BER. The result of above eq (13) can be evaluated numerically given the predicted channel coefficient $\widehat{H}$, the MMSE of prediction σ^2, the constellation, the noise power, and the free Hamming distance of convolution encoder. We refer to this method as an ABICM scheme based on the Expurgated bound. Above Equation (13) is used to compute the thresholds for adaptive modulation. Note that it is too complex to be computed in real time due to the rapidly-varying channel conditions. However, it is possible to compute the thresholds offline and to employ a look-up table in mobile communication equipment in practice. The computational speed of $E_{\widehat{H}(m)}$ is much higher than for simulations-based methods, which are often used to determine the thresholds in complex adaptive modulation systems and need to run millions of bits to obtain reliable results.

IV. Numerical Results

IV. (i) BER Comparison

First, we investigate the BER achieved by the original method and our ABICM method for the original ABICM method, two nominal schemes that employ quadrature phase shift keying (QPSK) and 64QAM in Rician fading channel are used, and the resulting D_0 values are 0.0367 and 0.0624, respectively. Fig: 1 show the simulated BER vs. prediction range for the two ABICM methods. In practical mobile communication systems, the prediction range is usually $0.1 - 0.5\lambda$. Within this prediction range, the BER of the original ABICM method is either significantly greater or lower than the target BER depending on the choice of the nominal scheme. Moreover, the resulting BER of the original BICM method with AWGN, ABICM method based on Expurgated Bound with Perfect CSI conditions, ABICM method based on Expurgated Bound with Rayleigh Channel varies dramatically as the prediction range changes. On the other hand, the method based on the Expurgated Bound with Rician Fading Channel maintains the target or Better BER. Results in confirm this conclusion for other SNR values. In wireless communication system design, it is desirable to obtain as accurate estimate of the BER as possible. While the original ABICM method sometimes achieves a lower BER than the target BER, a system designer would prefer to save the transmission power by maintaining the BER at a higher but acceptable rate. Therefore, we employ our ABICM method in the simulations.

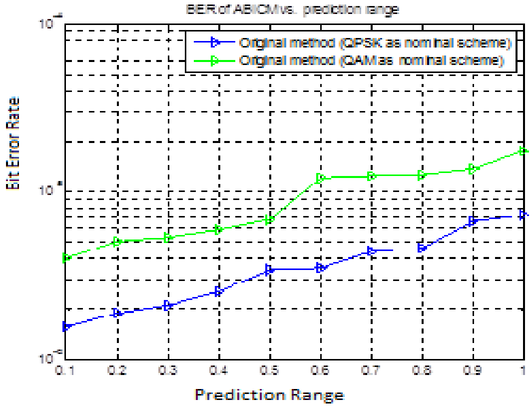

Fig: 1 BER of ABICM vs. prediction range For the Rician Fading Channel

IV.(ii) Spectral Efficiency Comparison

Fig: 2(i) and (ii) Compares the spectral efficiency of several methods for different SNR values and CSI reliability. Two prediction MMSE values are considered, σ2 = 0.1 and 0.001, which for fdm = 200 Hz correspond to 2ms (0.4λ) and 0.1ms (0.2λ) prediction ranges at 30dB SNR .When CSI is reliable (σ2 = 0.001), ATCM achieves the highest spectral efficiency for medium to high SNR since its minimum Euclidean distance is larger. On the other hand, the spectral efficiency of ATCM is significantly degraded by imperfect CSI, while ABICM still maintains high spectral efficiency for σ2 = 0.1, a typical MMSE for realistic mobile radio conditions. Both ABICM and ATCM outperform uncoded adaptive modulation, although the coding gain of ATCM is small when the CSI is not reliable. Note that ABICM significantly outperforms these non-adaptive schemes. This comparison demonstrates that in the slow fading channel adaptive modulation methods that do not require interleaving, e.g., ATCM, achieve the best spectral efficiency. On the other hand, ABICM is the best choice for practical mobile wireless channels.

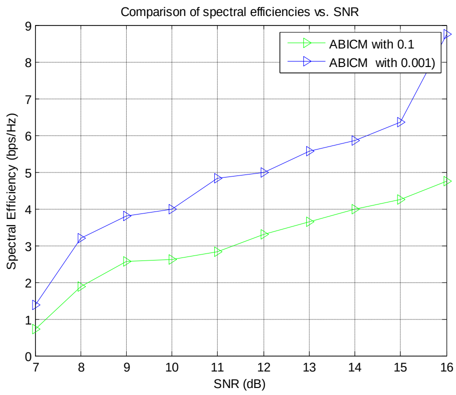

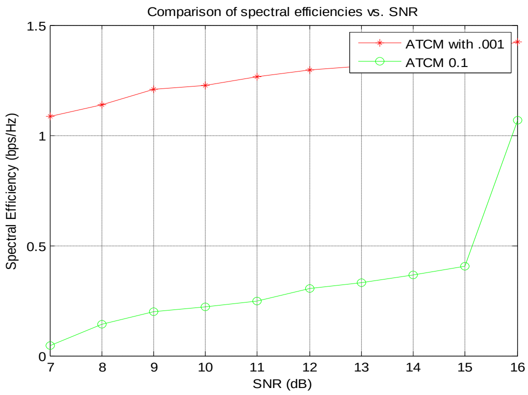

Fig: 2(i) **Fig: 2(ii)**

Fig: 2(i), (ii) Comparison of spectral efficiencies vs. SNR for prediction accuracies σ^2 = 0.001 and σ^2 = 0.1 for ABICM, ATCM for Rician Fading Channel

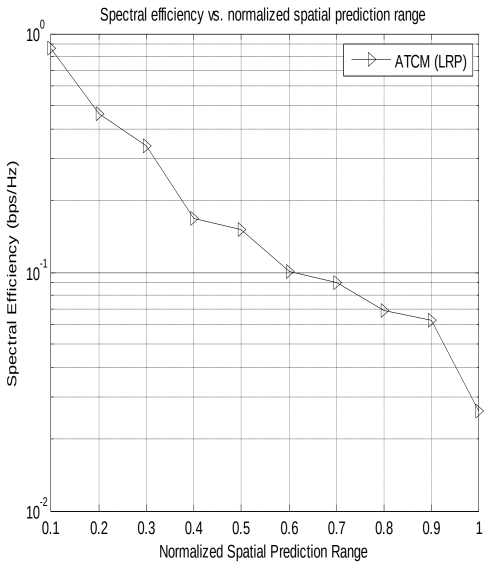

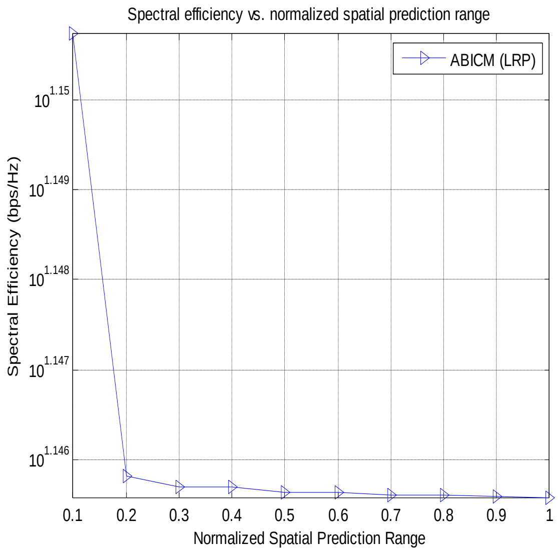

Fig:3 (i) **Fig: 3(ii)**

Fig: 3(i), (ii) Spectral Efficiency vs. Normalized Spatial Prediction Range for ATCM and ABICM for Rician Fading Channel

Fig: 3 (i), (ii) illustrates the dependency of the spectral efficiency on the normalized spatial prediction range $f_{dm}\tau$. Fig: 4 Compares the performance of rate R = 2/3 convolution codes with different constraint lengths K. Increasing K from 2 to 4 results in spectral efficiency improvement of 0.3-0.6 bps/Hz. The spectral efficiency loss due to imperfect CSI (σ^2 = 0.1) relative to σ^2 = 0 is smaller for K = 4 than for K = 2. Thus in addition to higher coding gain, longer constraint length K provides better protection against prediction errors by spreading the bits associated with the poor channel predictions. This figure also shows that even for imperfect CSI ABICM outperforms the non-adaptive BICM scheme with the same convolution encoder.

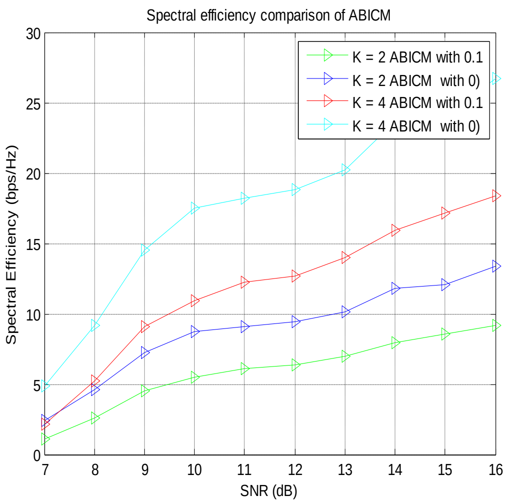

Fig: 4 Spectral efficiency comparision of ABICM : rate 2/3 Convolution Code with Different Constraint lengths K=2,4 corresponding to SNR for Rician Fading Channel

V. CONCLUSION

In this paper, we investigated ABICM aided by fading prediction for OFDM systems. New ABICM method based on the expurgated bound was developed and shown to achieve much better BER accuracy relative to the method originally proposed for ABICM with imperfect CSI. It was demonstrated that ABICM is much less sensitive to CSI errors than ATCM and un coded adaptive modulation, but reliable fading prediction is required to enable ABICM for realistic mobile radio systems. A possible future extension of this work is to investigate utilization of the variable-rate Turbo BICM [19] in the rapidly fading environment.

REFERENCES

[1] P. Ormeci, X. Liu, D. L. Goeckel, and R. D. Wesel, "Adaptive bit interleaved coded modulation," IEEE Trans. Commun.,vol.49,no.9,pp. 1572–1581, Sep. 2001.

[2] T. Jia, "Single and multicarrier adaptive transmission systems with long-range prediction aided by noise reduction," Ph.D. dissertation, NC State University, Raleigh, NC, 2008.

[3] V. K. N. Lau, "Performance analysis of variable rate: symbol-by-symbol adaptive bit interleaved coded modulation for Rayleigh fading channels,"IEEE Trans. Veh. Technol., vol. 51, no. 3, pp. 537–550, May 2002.

[4] K. Song, A. Ekbal, S. T. Chung, and J. M. Cioffi, "Adaptive modulationand coding (AMC) for bit-interleaved coded OFDM (BIC-OFDM),"IEEE Trans. Wireless Commun., vol. 5, pp. 1685–1694, July 2006.

[5] G. Caire, G. Taricco, and E. Biglieri, "Bit-interleaved coded modulation," IEEE Trans. Inf. Theory, vol. 44, no. 3, pp. 927–946, May 1998.

[6] A. Duel-Hallen, S. Hu, and H. Hallen, "Long-range prediction of fadingsignals," IEEE Signal Process. Mag., vol. 17, no. 3, pp. 62–75, May2000.

[7] A. Duel-Hallen, "Fading channel prediction for mobile radio adaptive transmission systems," Proc. IEEE, vol. 95, pp. 2299–2313, Dec. 2007.

[8] A. J. Goldsmith and S.-G. Chua, "Adaptive coded modulation for fading channels," IEEE Trans. Commun., vol. 46, no. 5, pp. 595–602, May1998.

[9] T. Jia, A. Duel-Hallen, and H. Hallen, "Improved long-range prediction with data-aided noise reduction for adaptive modulation systems," inProc. 2008 Conference on Information Sciences and Systems.

[10] "Performance of adaptive coded modulation enabled by long-range fading prediction with data-aided noise reduction," in Proc. 2008IEEE MILCOM.

[11] J. Campello, "Optimal discrete bit loading for multicarrier modulation systems," import. 1998 IEEE ISIT, p. 193

[12] A. J. Goldsmith and S.-G.Chua, "Variable-rate variable-power MQAMfor fading channels," IEEE Trans. Commun., vol. 45, no. 10, pp. 1218–1230, Oct. 1997.

[13] S. Falahati, A. Svensson, T. Ekman, and M. Sternad, "Adaptive modulation systems for predicted wireless channels," IEEE Trans. Commun.,vol. 52, pp. 307–316, Feb. 2004.

[14] S. Falahati, A. Svensson, M. Sternad, and H. Mei, "Adaptive trelliscoded modulation over predicted flat fading channels," inProc. 2003 IEEE VTC, vol. 3, pp. 1532–1536.

[15] D. L. Goeckel, "Adaptive coding for time-varying channels usingoutdated fading estimates,"IEEE Trans. Commun., vol. 47, no. 6, pp.844–854, July 1999.

[16] E. Biglieri, G. Caire, G. Taricco, and J. Ventuura, "Simple method forevaluating error probabilities," Electron.Lett., vol. 32, no. 3, pp. 191–192, Feb. 1996.

[17] J. Proakis, Digital Communications, 4th edition.McGraw-Hill, 2001.

BIOMETRIC RECOGNITION USING MULTIMODAL TECHNOLOGY

Priya Yadav[1],Gauri Singh[2],Gladish Swain[3],Pragati Srivastava[4]

[1,2,3,4]*Department of Computer science Engineering,DCE gurgaon(India)*

ABSTRACT

Biometric is expressed as the science of identifying an individual on the basis of their physiological or behavioral traits. It seems to achieve acceptance as a rightful method for ob-taining an individual's identity. Multimodal biometric systems are widely used for different security applications. Major usage of such systems is in authentication and identification purpose, for example, authorized access control or terrorist identification, unique identity for human being etc.

Keywords: Biometrics, , DNA Recognition, Fingerprint Recognition , Iris Recognition

I. INTRODUCTION

Biometric is expressed as the science of identifying an individual on the basis of their physiological or behavioral traits. It seems to achieve acceptance as a rightful method for obtaining an individual's identity . Biometric systems possess numerous advantages like, it is difficult to share and reproduce, it is user friendly. i.e. there is no need to remember long and random passwords, it cannot be obtained by direct observation and it safe-guards against repudiation by the user.

Biometric systems that generally utilize a single attribute for recognition are influenced by some practical issues like noisy in sensor data, non-universality and/or lack of distinctiveness of the biometric trait . Multimodal biometric systems prevail over some of these issues by strengthening the proof acquired from several sources. It is believed that to enhance the performance of the sys-tem by providing more valuable information to the classifier. Bio-metric traits are acquired from multiple sources to recognize a per-son. Different characteristics can be examined by a single system or separate systems that functions on its own and their decisions can be merged together

This paper focuses on the feature level fusion approach for creating multibiometric template due to two reasons: (i) it provides synergetic (complimentary) information for identification and (ii) it contains raw data (more information) as compared to decision level . This work investigates the feasibility of creating a single multibiometric template using similarity measure.

The fingerprints and irises decompose very soon after the death of a person but the DNA sequence never decomposes. Thus, it is always important to use fingerprints, iris image, and DNA features based multimodal system for identifying a dead and an alive person. Hence, we have reviewed and analyzed the performance of fingerprints, iris, and DNA features based multimodal systems in this research work.

II. IRIS RECOGNITION SYSTEM

The iris is a thin, circular structure in the eye, responsible for controlling the diameter and size of the pupil and thus the amount of light reaching the retina. The color of the iris is often referred to as eye color.A front on-view of the iris is as shown in the figure below

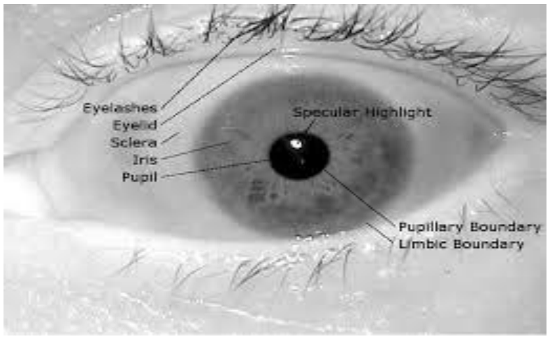

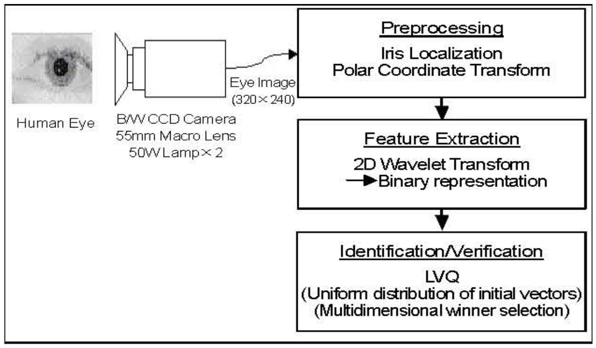

Fig1:Eyes structure **Fig2:Structure of proposed iris recognition system**

Iris based identification is secure and accurate because, iris image doesn't change for the whole life of a person. The iris image fully develops in the first six months after the birth of a child. An Iris based identification system includes following four basis steps for identifying a person:

Step 1: Image Acquisition means capturing the iris Image using a high resolution camera.

Step 2:Image Preprocessing includes converting the image to a gray scale image and removing noise disturbances.

Step 3:Template matching compares the user templates with templates of database using a matching metric

Step 4: Authentication uses the matching metric and declares a person either an authentic person or an imposter.

III. FINGERPRINTING SYSTEM

Fingerprint based systems describes the state-of-the-art of fingerprints based identification methods with advantages, disadvantages, and key features comparison. Traditionally, tokens such as physical key, personal ID cards, and passwords were used to identify a person. The various limitations of these automatic tokens are:

Fingerprints include the ridge, furrows, minutiae points, orientation of minutiae points, distances between minutiae points, whorl, and curves of fingerprints. Hand geometry based identification approaches use the geometric form of hand for confirming the identity of a person. Although, human hands are not unique but, few essential features such as hand length, finger length, finger width, palm length, and palm width may differ from one person to another person. In hand geometry based identification method the hand image is captured using a CCD camera for feature extraction. In image pre-processing stage we extract the hand silhouettes and eliminate artifacts such as guidance pins; user rings; and overlapping cuffs. In hand silhouettes alignment we compute hand length, finger length, finger width, palm length, and palm width. The matching module compares user features with templates stored in database and generates the matching score.

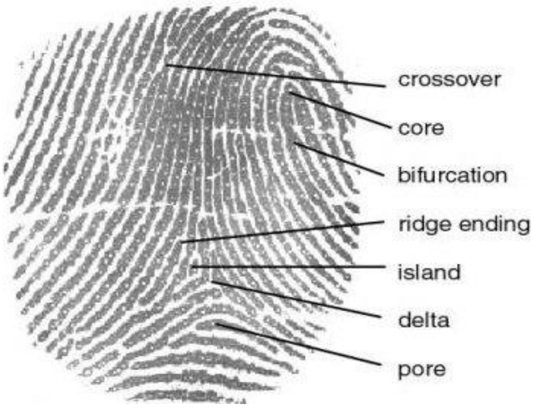

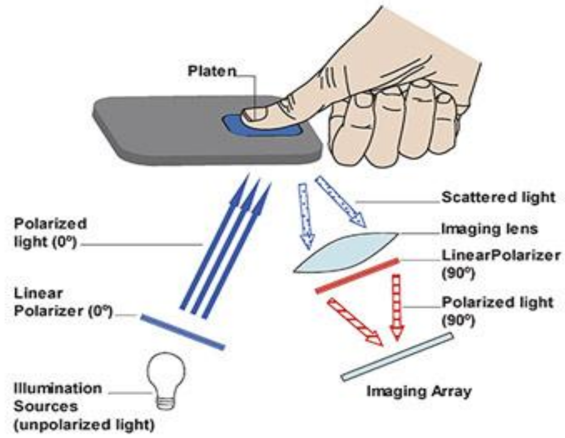

Fig3:Structure of human thumb **Fig4: Proposed finger recognition system**

The three basic patterns of fingerprint ridges are the arch, loop, and whorl:

- arch: The ridges enter from one side of the finger, rise in the center forming an arc, and then exit the other side of the finger.
- loop: The ridges enter from one side of a finger, form a curve, and then exit on that same side.
- whorl: Ridges form circularly around a central point on the finger.
-

IV. DNA RECOGNITION SYSTEM

Deoxyribonucleic acid (DNA) is the one-dimensional (1–D) ultimate unique code for one's individuality—except for the fact that identical twins have identical DNA patterns

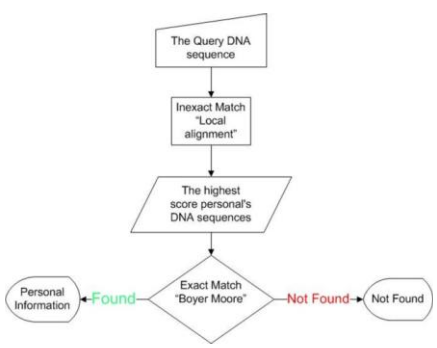

Fig5: Proposed DNA recognition system

V. MULTIMODAL BIOMETRIC SYSTEM

Multimodal biometric systems consolidate the evidence presented by multiple biometric sources and typically provide better recognition performance compared to systems based on a single biometric modality. Although information fusion in a multimodal system can be performed at various levels, integration at the matching score level is the most common approach due to the ease in accessing and combining the scores generated by different matchers. Since the matching scores output by the various modalities are heterogeneous, score normalization is needed to transform these scores into a common domain, prior to combining them.

VI. LEVELS OF FUSION

A generic biometric system has 4 important modules: (a) thesensor module which captures the *trait* in the form of rawbiometric *data*;

(b) the feature extraction module which processes the data to extract a *feature set* that is a compact representationof the trait;

(c) the matching module which employs a classifier to compare the extracted feature set with the templatesresiding in the database to generate matching scores;

(d) the decision module which uses the matching scores to either determine an identity or validate a claimed identity.

In amultimodal biometric system informationreconciliation canoccur in any of the aforementioned modules

(a) Fusion at the data or feature level: Either the data itself orthe feature sets originating from multiple sensors/sources arefused.

(b) Fusion at the match score level: The scores generatedby multiple classifiers pertaining to different modalitiesare combined.

(c) Fusion at the decision level: The final output1 of multiple classifiers are consolidated via techniques such as majority voting [5].

Biometric systems that integrate information at an early stage of processing are believed to be more effective than those systems which perform integration at a later stage. Since the feature set contains richer information about the input biometric data than the matching score or the output decision of a matcher, fusion at the feature level is expected to provide better recognition results. However, fusion at this level is difficult to achieve in practice because the feature sets of the various modalities may not be compatible

VII. DESIGN ISSUES

A variety of factors should be considered when designing a multimodal biometric system. These include

(a) the choice and number of biometric traits, (b) the level in the biometric system at which information provided by multiple traits should be integrated,

(c) the methodology adopted to integrate the information, and

(d) the cost versus matching performance trade off.

The choice and number of biometric traits is largely driven by the nature of the application, theoverhead introduced by multiple traits (computational demands and cost, for example), and the correlation between the traits considered (uncorrelated information is preferred since the performance improvement is more pronounced in this case). In a cell phone that is equipped with a camera, it might be easier to combine the face and voice traits of a user, while in an ATM application it might be easier to combine the fingerprint and face traits of the user. In identification systems comprising of a large number of users (in the order of millions), an indexing mechanism may be facilitated using a multimodal approach [15]. Researchers are currently studying the performance gain that can be obtained using state-of-the-art commercial off-the-shelf (COTS) fingerprint and face systems, on a large population of individuals [19].

VIII. CASCADED MULTIBIOMETRIC SYSTEM

• Capture biometric measurements as needed

(Sequential pattern recognition)

• Verification - reduces the average verification time

• Identification - successively prunes the database (indexing)

• To reduce the average verification time, the modalities must be cascaded in the decreasing order of accuracy

• In user-friendly systems, the user can be allowed tochoose the order of the modalities

IX. SUMMARY AND CONCLUSIONS

Multimodal biometric systems elegantly address several of the problems present in unimodal systems. By combining multiple sources of information, these systems improve matching performance, increase population coverage, deterspoofing, and facilitate indexing. Various fusion levels and scenarios are possible in multimodal systems. Fusion at the match score level is the most popular due to the ease in accessing and consolidating matching scores. Performance gain is pronounced when uncorrelated traits are used in a multimodal system. Incorporating user-specific parameters can further improve performance of these systems. the widespread deployment of biometric systems in several civilian and government applications, it is only a matter of time before multimodal biometric systems begin to impact the way in which identity is established in the 21st century

REFERENCES

[1] D. Sarunyagate, Ed., *biometrics*. New York: McGraw-Hill, 1996.

[2] G. O. Young, "Synthetic structure of industrial biometrics," in, 2nd ed., vol. 3, J. Peters, Ed. New York: McGraw-Hill, 1964, pp. 15-64.

[3] User’s guide: Microsoft word vers. 5.0, Microsoft,1991.

[4] “BIOMETRICS,” Encyclopedia brittanica, 1984 ed.

REVIEWS ON THE EFFECTS OF FRICTION STIR WELDING PARAMETERS ON MECHANICAL PROPERTIES OF DISSIMILAR METAL WELD JOINTS

Er. Jagjeet Singh Chatha
Department Of Mechanical Engineering, Punjab Technical University Giani Zail Singh Campus, Bathinda, Punjab, (India)

ABSTRACT

Friction stir welding is a solid state welding technique which produces high quality welds even in difficult to weld materials such as aluminum, brass, copper and others such material . It was invented in 1991 by the welding institute. This technique produces a very good quality weld joint without actual melting of the materials. The technique is fast, environmentally friendly and simple to perform. In addition, a lot of Industry applications exist for friction stir welded components. The scope of the present investigation is to evaluate the effects of friction stir welding parameters on mechanical properties of dissimilar metal weld joints. From this review it has been found that the welding parameters like Tool Rotation Speed, Feed rate, Tool Tip Shape, Tool Tip Plunge Depth, Tool Tilt Angle, Shoulder Diameter are greatly influence the mechanical properties of friction stir welded joints. Further scope of carrying-out work was also discussed in this review paper.

Keywords: Friction Stir Welding (FSW), Dissimilar Metals, Mechanical Properties, Tool Rotation Speed, Feed Rate, Tool Tip Plunge Depth

I. INTRODUCTION

In recent world a pressure of producing stronger and lighter products while using less energy and doing less environmental harm with lower cost and in short time increased. Many problems associated with traditional fusion welding techniques such as shrinkage, solidification cracking and porosity becomes big obstacle in meeting the standards which leads to more wasting of material, time and money. To overcomes many such problems, a need of new welding technology arise which develops friction stir welding technique. Friction Stir welding technique was invented by Wayne Thomas at The Welding Institute Ltd in 1991. Friction stir welding is a solid state process which produces high quality welds even in difficult to weld materials such as aluminum, brass, copper and others. Friction stir process has received world-wide attention, and today it is used for production in many sectors like aerospace, railway, automotive, shipbuilding, heat exchangers, and nuclear waste containers. In friction stir welding process the material to be welded is clamped tightly, than the tool is plunged in work piece which is to be welded at certain angle until the tool shoulder touches the surface of the work piece in the centre line. The friction stir welding process consists of pin and the shoulder. The material used as a rotating tool is harder than the material to be welded. Once the tool is plunged in, then it is rotated for certain time without any feed for required heat generation and this time is called indentation time, when required heat is generated the feed is given. Due to raise of temperature the material gets soften and flow towards the tool rotating direction and weld occurs. The critical process parameters which affect the weld joint produced using friction stir welding are Tool Rotation Speed, Travelling Feed/Feed rate, Tool Tip Shape, Tool Tip Plunge Depth, Tool Tilt Angle, Shoulder Diameter [1, 2, 3]. In the current study researches from various authors has been reviewed.

II. LITERATURE REVIEW

Ranjith R., Senthil Kumar B. [2014] investigated joining of two dissimilar aluminium alloys AA2014 T651 and AA6063 T651 using friction stir welding. The experiments were conducted on vertical end milling machine. The friction stir tool is of high speed steel with various pin diameter 5mm, 6mm and 7mm respectively. The friction stir pin length is 5.8mm and diameter of the shoulder is 20mm. The tool has the constant rotational speed of 2000rpm and welding feed of 16mm/min. The tool was rotated in the clock wise direction and tilt angle of the tool was varied between 3 to 5 degrees. Tensile strength, Optical microscope and %Elongation was carried out to evaluate the weld. It is observed that 6 mm pin diameter, 4 degree tilt angle and 0.5 mm offset towards advancing side give the optimum tensile strength of 371 MPa [3].

R. Hariharan, R.J. Golden and Renjith Nimal. [2013] investigated the development of friction stir welded joint of dissimilar aluminum alloys (6061 and 7075) by using Computerized Numerical Control Machine and also compared the effect of tapered pin and cylindrical pin type tools on tensile strength of aluminum alloys (6061 and 7075).The main process parameters considered are rotation speed (1600 and 1250rpm), traverse speed (120mm/min) and tool tilt angle 2^0. The weld joint is evaluated with micro-structure, hardness, and tensile testing. The results demonstrated that the tensile strength of tapered pin sample was around 30% and 15% higher than cylindrical one at 1250rpm and 1600rpm respectively. The maximum tensile strength value (485Mpa) is obtained at rotation speed of 1250 rpm, welding speed of 120 mm/min and tool angle 2 degree tilt. It is also observed that with increase in tool rotation speed the tensile value also increase till critical level and then decline. It is suggested to select taper pin as tool and optimize parameters for a sound welding of dissimilar material [4].

K.Satheesh kumar, G.Rajamurugan, P.Manikkavasagan. [2013] investigated the joining of dissimilar aluminium AA6061 and AA7075 6mm thickness plates by friction stir welding. The process parameters used are rotational speed and transverse feed of 1200, 1400, 1600 rpm and 20, 35, 50 mm/min at constant axial force 5kN. The effect of friction stir welding parameter was evaluated by performing micro-structure, hardness and tensile testing. The rotational speed of 1600rpm and feed of 35mm/min gives the maximum tensile strength. The lower rotational speed leads decline of tensile strength [5].

Muhamad Tehyo, Prapas Muangjunburee, Abdul Binraheem, Somchai Chuchom and Nisida Utamarat. [2012] investigated the effect of friction stir welding parameters on the microstructure and mechanical properties friction stir welded butt joints of dissimilar aluminum alloy sheets between Semi-Solid Metal (SSM) 356-T6 and AA6061-T651 using computerized numerical control machine. The two main parameters considered are tool rotation speeds (1,750 and 2,000 rpm) and six welding speeds (20, 50, 80, 120, 160, and 200 mm/min). The results are evaluated with help of microstructure, hardness and tensile testing. The maximum tensile strength of 206.3 MPa was derived from a welded specimen produced at the tool rotation speed of 2,000 rpm associated with the welding speed of 80 mm/min. As the tool rotation speed and welded speed increases the tensile result improve till it reach maximum value, further increase leads in fall of tensile strength[6].

R.Madhusudhan, M.M.M.Sarcar, N.Ramanaiah, K.Prasada Rao. [2012] investigated the effect of friction stir welding parameters on mechanical and micro structural properties of friction stir weld joint of dissimilar aluminium alloy (AA 6262-T6 and AA 7075-T6). The main parameters varied are Tool Rotational Speed(1000,1200, 1400 rpm), Weld Speed(0.4,0.6, 0.8 mm/sec), Axial Force (8,9,10 kN), Tool shoulder diameter (18 mm), Tool Pin swept diameter (6 mm), Pin Length (5.8 mm). The weld joint is evaluated by optical microscopy, hardness and tensile strength testing. The better mechanical properties (hardness and tensile strength) were obtained at joint fabricated with 1200 rpm tool rotational speed, 0.6 mm/sec weld speed and 9kN axial force compared to all other conditions [7].

R. Palanivel, P. Koshy Mathews. [2011] investigated the tensile behaviour of friction-stir- welded dissimilar aluminium alloys (AA6351-T6 to AA5083-H111). The five different tool pin profiles were used welding, such as Tapered Square, Straight Square, Straight Hexagon, Tapered Octagon and Straight octagon in addition with three different welding speeds (50 mm/min, 63 mm/min and 75 mm/min). The tensile test was performed to evaluate the joint and it was observed that the highest tensile strength value was obtained with straight square tool pin at 75mm/min welding speed. The increase in welding speed leads to an increase in the tensile strength up to a maximum value, while a further increase results in a decrease of the tensile strength [8].

Yan Yong, Zhang Da-Tong, Qiu Cheng, Zhang Wen. [2010] investigated the dissimilar friction stir welding between 5052 Al alloy and AZ31 Mg alloy with the plate thickness of 6 mm. The best results were observed at rotation speed of 600 r/min and welding speed of 40 mm/min. As compared with the micro-structure of base materials, the microstructure of the stir zone is greatly refined. Complex flow pattern characterized by intercalation lamellae is formed in the stir zone. Micro-hardness value presents an uneven distribution due to the complicated micro-structure at the weld joint, and is twice higher than that of the base materials. The tensile fracture position locates at the aluminum side where the hardness value of weld joint shows a sharp decrease from the stir zone to 5052 base material [9].

Z. Barlas, H. Uzun. [2008] investigated Microstructure and mechanical properties of friction stir butt welded dissimilar Copper and brass sheets. The commercial pure copper (Cu) and brass (CuZn30) sheets which have dimension 150 mm length, 100 mm width and 3 mm thickness were friction stir welded. The main process parameters considered are tool rotational speed with the clockwise (800 rpm), travel speed (22 mm/min) and the tool axis was tilted at 3^0. In order to evaluate the joint performance and the weld zone characteristics, the microstructure, micro-hardness, tensile and bending tests are conducted. : The tensile strength of joints was found to be about same and 46% lower than that of Cu parent metal and CuZn30 respectively. It is demonstrated that commercial pure copper can be successfully joined to dissimilar CuZn30 alloy using friction stir welding [10].

III. CONCLUSIONS

Following points can be concluded from the literature review.

- The Friction stir welding is a successful technique to join dissimilar alloy like aluminum, copper and brass.

- A higher tool rotation speed resulted in a higher tensile strength till the maximum value, further increase results in decline in tensile value.
- Optimum friction stir welding parameters should be properly selected for good results.
- The heat input increases as the tool rotational speed increases
- No addition material or fillers are required for welding.
- It is the environment friendly welding technique as no harmful emissions from the process.
- The increase in welding speed results in increase in tensile strength up to a maximum value, further increase results in a decrease of the tensile strength

IV. FUTURE SCOPE

As majority of the research studies on Friction Stir Welding has been done by taking one or two factor at a time which provides results by involves hit and trial methodology. So the combined effect of various parameters like tool rotation speed, tool profile, tool tilt angle, welding speed etc can be investigated for different materials which will give more accurate and detailed results.

REFERENCES

[1] H.M.Anil Kumar, Dr. V. Venkata Ramana(2014), "An Overview of Friction Stir Welding (FSW): A New Perspective". Research Inventy: International Journal of Engg. And Sci.Vol.4, Issue 6.

[2] Rahul Singla, Bikram Jit Singh (2014), "Doe: A Key to Optimize Friction Stir Welding of Dissimilar Aluminum Alloys". (IJERA) ISSN: 2248-9622

[3] Ranjith R., Senthil Kumar B(20140, "Joining of dissimilar aluminium alloys AA2014 T651 and AA6063 T651 by friction stir welding process". E-ISSN: 2224-3429, Volume 9.

[4] R. Hariharan, R.J. Golden and Renjith Nimal(2013), "Friction Stir Welding Oof Dissimilar Aluminium Alloys (6061 and 7075) By Using Computerized Numerical Control Machine". Middle-East J. Sci. Res., 14 (12): 1752-1756.

[5] K.Satheesh kumar, G.Rajamurugan, P.Manikkavasagan(2013) ,"Effect of process parameters on friction stir welding of dissimilar Aluminium Alloy". (IOSR-JMCE) e-ISSN: 2278-1684, p-ISSN: 2320-334X.

[6] Muhamad Tehyo, Prapas Muangjunburee, Abdul Binraheem, Somchai Chuchom and Nisida Utamarat(2012), "Influence of friction stir welding parameters on metallurgical and mechanical properties of dissimilar joint between semi-solid metal 356-T6 and aluminum alloys 6061-T651". Songklanakarin J. Sci. Technol. 34 (4), 415-421.

[7] R. Palanivel, P. Koshy Mathews(2011), "The tensile behaviour of friction-stir- welded dissimilar aluminium alloys". Materials and technology 45 (2011) 6, 623–626.

[8] Yan Yong, Zhang Da-Tong, Qiu Cheng, Zhang Wen(2010), "Dissimilar friction stir welding between 5052 aluminum alloy and AZ31 magnesium alloy". Trans. Nonferrous Met. Soc. China 20(2010) s619−s623.

[9] Z. Barlas, H. Uzun(2008), "Microstructure and mechanical properties of friction stir butt welded dissimilar Cu/CuZn30 sheets".JAMME,Volume 30 Issue 2.

DESIGN AND MODELING OF FUZZY CONTROLLED SVC FOR QUALITY ENHANCEMENT IN TRANSMISSION LINE

[1]P.Gani Raju, [2]Praveen Kumar Mishra

[1,2] Electrical and Electronics Engineering, OPJIT Raigarh, CG, India

ABSTRACT

Flexible AC transmission system (FACTS) is a technology, which is based on power electronic devices, used to enhance the existing transmission capabilities in order to make the transmission system flexible and independent operation. The FACTS technology is a promising technology to achieve complete deregulation of Power System i.e. Generation, Transmission and Distribution as complete individual units. The loading capability of transmission system can also be enhanced nearer to the thermal limits without affecting the stability. Complete close-loop smooth control of reactive power can be achieved using shunt connected FACTS devices. Static VAR Compensator (SVC) is one of the shunt connected FACTS device, which can be utilized for the purpose of reactive power compensation. Intelligent FACTS devices make them adaptable and hence it is emerging in the present state of art. This paper attempts to design and simulate the Fuzzy logic control of firing angle for SVC in order to achieve better, smooth and adaptive control of reactive power. The design, modeling and simulations are carried out for λ /8 Transmission line and the compensation is placed at the receiving end (load end).

Keyword- Fuzzy Logic, FACTS and SVC

I. INTRODUCTION

The reactive power generation and absorption in power system is essential since the reactive power is very precious in keeping the voltage of power system stable. The main elements for generation and absorption of reactive power are transmission line, transformers and alternators. The transmission line distributed parameters throughout the line, on light loads or at no loads become predominant and consequently the line supplies charging VAR (generates reactive power). In order to maintain the terminal voltage at the load bus adequate, reactive reserves are needed. FACTS devices like SVC can supply or absorb the reactive power at receiving end bus or at load end bus in transmission system, which helps in achieving better economy in power transfer. In this paper Transmission line (λ /8) is simulated using 4π line segments by keeping the sending end voltage constant. The receiving end voltage fluctuations were observed for different loads. In order to maintain the receiving end voltage constant, shunt inductor and capacitor is added for different loading conditions. SVC is simulated by means of fixed capacitor and thyristor controlled reactor (FC-TCR) which is placed at the receiving end. The firing angle control circuit is designed and the firing angles are varied for various loading conditions to make the receiving end voltage equal to sending end voltage. Fuzzy logic controller is designed to achieve the firing angles for SVC such that it maintains a flat voltage profile. All the results thus obtained, were verified and were utilized in framing of fuzzy rule base in order to achieve better reactive power compensation for the Transmission line (λ/8). Based on observed results for load voltage variations for different values of load resistance, inductance and capacitance a fuzzy controller is designed which controls the firing angle of SVC in order to automatically maintain the receiving end voltage constant.

II. OPERATING PRINCIPLES AND MODELING OF SVC

An elementary single phase thyristor controlled reactor [1] (TCR) shown in Fig.1 consists of a fixed (usually air core) reactor of inductance L and a two anti parallel SCRs. The device brought into conduction by simultaneous application of gate pulses to SCRs of the same polarity. In addition, it will automatically block immediately after the ac current crosses zero, unless the gate signal is reapplied. The current in the reactor can be controlled from maximum (SCR closed) to zero (SCR open) by the method of firing delay angle control. That is, the SCR conduction delayed with respect to the peak of the applied voltage in each half-cycle, and thus the duration of the current conduction interval is controlled. This method of current control is illustrated separately for the positive and negative current cycles in Fig.2 where the applied voltage V and the reactor current $iL(\alpha)$ at zero delay angle (switch fully closed) and at an arbitrary α delay angle are shown. When α =0, the SCR closes at the crest of the applied voltage and evidently the resulting current in the reactor will be the same as that obtained in steady state with a permanently closed switch. When the gating of the SCR is delayed by an angle α $(0 \le \alpha \le \pi/2)$ with respect to the crest of the voltage, the current in the reactor can be expressed [1] as follows

$$V(t) = V \cos \omega t. \qquad (1)$$

$$i_L = (1/L) \int_{\alpha}^{\omega t} V(t)dt = (V/\omega L)(\sin \omega t - \sin \alpha) \qquad (2)$$

Since the SCR, by definition, opens as the current reaches zero, is valid for the interval $\alpha \le \omega t \le \pi - \alpha$. For subsequent negative half-cycle intervals, the sign of the terms in equation (1) becomes opposite.

In the above equation (1) the term $(V/\omega L) \sin \alpha = 0$ is offset which is shifted down for positive and up for negative current half-cycles obtained at $\alpha = 0$, as illustrated in Fig.2. Since the SCRs automatically turns off at the instant of current zero crossing of SCR this process actually controls the conduction intervals (or angle) of the SCR. That is, the delay angle α defines the prevailing conduction angle σ ($\sigma = \pi$-2α). Thus, as the delay angle α increases, the corresponding increasing offset results in the reduction of the conduction angle σ of the SCR, and the consequent reduction of the reactor current. At the maximum delay of $\alpha = \pi/2$, the offset also reaches its maximum of $V/\omega L$, at which both the conduction angle and the reactor current becomes zero. The two parameters, delay angle α and conduction angle σ are equivalent and therefore TCR can be characterized by either of them; their use is simply a matter of preference. For this reason, expression related to the TCR can be found in the literature both in terms of α and σ [1].

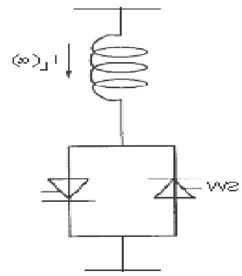

Fig. 1. Basic Thyristor Controlled Reactor

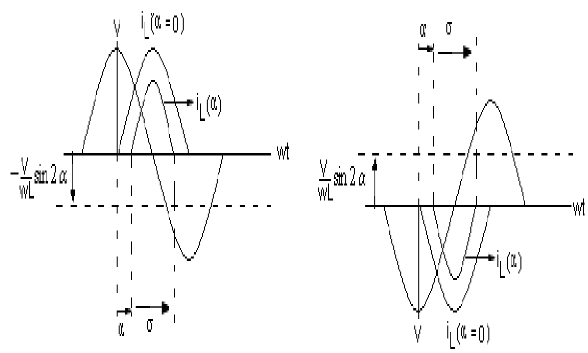

Fig.2. firing delay angle

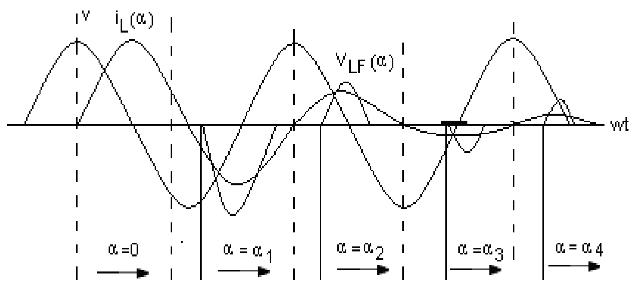

Fig. 3. Operating waveforms

It is evident that the magnitude of the current in the reactor varied continuously by delay angle control from maximum (α=0) to zero ($\alpha=\pi/2$) shown in Fig.3, where the reactor current $i_L(\alpha)$ together with its fundamental component $i_{LF}(\alpha)$ are shown at various delay angles α [1]. However the adjustment of the current in reactor can take place only once in each-half cycle, in the zero to $\pi/2$ interval [1]. This restriction result in a delay of the attainable current control. The worst-case delay, when changing the current from maximum to zero (or vice versa), is a half-cycle of the applied ac voltage. The amplitude $I_{LF}(\alpha)$ of the fundamental reactor current $i_{LF}(\alpha)$ can be expressed as a function of angle α [1].

$$I_{LF}(\alpha) = V/\omega L\,(1 - (2/\pi)\,\alpha - (1/\pi)\sin(2\alpha)) \qquad (3)$$

Where V is the amplitude of the applied voltage, L is the inductance of the thyristor-controlled reactor and ω is the angular frequency of the applied voltage. The variation of the amplitude $I_{LF}(\alpha)$, normalized to the maximum current I_{LFmax}, (I_{LFmax}= V/ωL), is shown plotted against delay angle α shown in Fig.4.

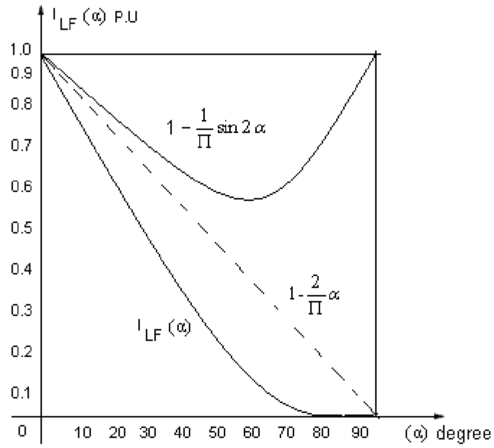

Fig.4. Amplitude variation of the fundamental TCR current with the delay angle (α)

It is clear from Fig.4 the TCR can control the fundamental current continuously from zero (SCR open) to a maximum (SCR closed) as if it was a variable reactive admittance. Thus, an effective reactance admittance, $B_L(\alpha)$, for the TCR can be defined. This admittance, as a function of angle α is obtained as:

$$B_L(\alpha)=1/\omega L(1-(2/\pi)\alpha-(1/\pi)\sin(2\alpha)) \qquad (4)$$

Evidently, the admittance $B_L(\alpha)$ varies with α in the same manner as the fundamental current $I_{LF}(\alpha)$.The meaning of equation (4) is that at each delay angle α an effective admittance $B_L(\alpha)$ can be defined which determines the magnitude of the fundamental current, $I_{LF}(\alpha)$, in the TCR at a given applied voltage V. In practice, the maximal magnitude of the applied voltage and that of the corresponding current limited by the ratings of the power components (reactor and SCRs) used. Thus, a practical TCR can be operated anywhere in a defined V-I area, the boundaries of which are determined by its maximum attainable admittance, voltage and current ratings as illustrated in the Fig.5a. The TCR limits are established by design from actual operating requirements. If the TCR switching is restricted to a fixed delay angle, usually α = 0, then it becomes a thyristor switched reactor (TSR). The TSR provide a fixed inductive admittance and thus, when connected to the ac system, the reactive current in it will be proportion to the applied voltage as the V - I plot in the Fig.5b.

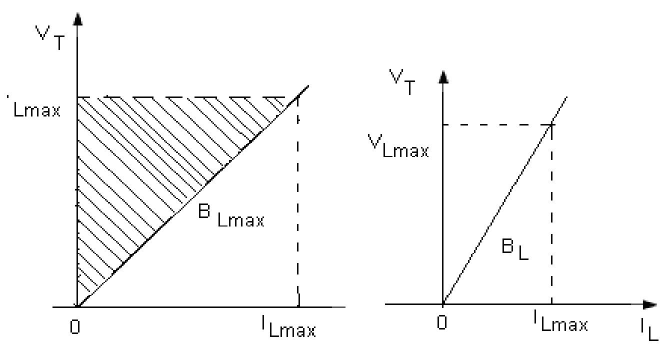

Fig.5. Operating V-I area of (a) For TCR and (b) For TSR

V_{Lmax} = voltage limit, I_{Lmax} = current limit

B_{Lmax} = max admittance of TCR,

B_L = admittance of reactor

A basic VAR generator arrangement using a fixed capacitor with a thyristor-controlled reactor (FC-TCR) shown in Fig.6 [1].The current in the reactor is varied by the previously discussed method of firing delay angle control. A filter network that has the necessary capacitive impedance at the fundamental frequency to generate the reactive power required usually substitutes the fixed capacitor in practice, fully or partially, but it provides low impedance at selected frequencies to shunt the dominant harmonics produced by the TCR. The fixed capacitor thyristor-controlled reactor type VAR generator may be considered essentially to consist of a variable reactor (controlled by a delay angle α) and a fixed capacitor. With an overall VAR demand versus VAR output characteristic as shown in Fig.7 in constant capacitive VAR generator (Q_c) of the fixed capacitor is opposed by the variable VAR absorption (Q_L) of the thyristor controlled reactor, to yield the total VAR output (Q) required. At the maximum capacitive VAR output, the thyristor-controlled reactor is off ($\alpha = 90^0$). To decrease the capacitive output, decreasing delay angle α. At zero VAR output increases the current in the reactor, the capacitive and inductive current becomes equal and thus the capacitive and inductive VARs cancel out. With a further decrease of angle α, the inductive current becomes larger than the capacitive current, resulting in a net inductive VAR output. At zero delay angle, the thyristor-controlled reactor conducts current over the full 180° interval, resulting in maximum inductive VAR output that is equal to the difference between the VARs generated by the capacitor and those absorbed by the fully conducting reactor.

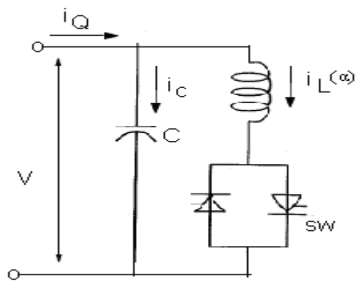

Fig.6. basic FC-TCR type static generator

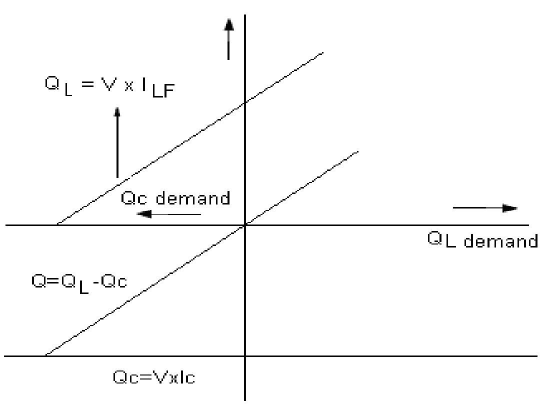

Fig.7. VAR demand versus VAR output characteristic.

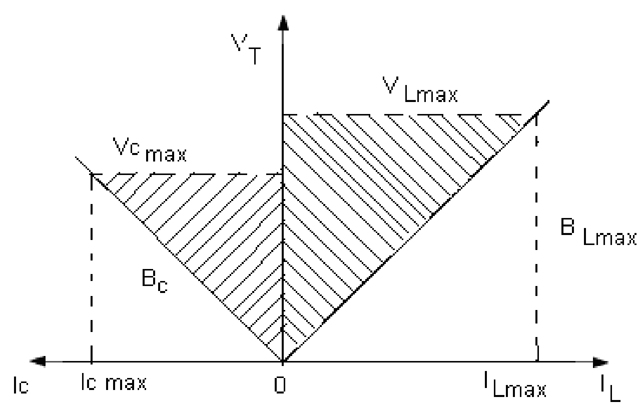

Fig.8. V-I characteristics of the FC-TCR type VAR Generator

In Fig.8 the [1] voltage defines the V-I operating area of the FC-TCR VAR generator and current rating of the major power components. In the dynamic V-I Characteristics of SVC along with the Load lines showed in the Fig.9[1] the load characteristics assumed straight lines for Dynamic studies as easily seen that the voltage improved with compensation when compared without compensation.

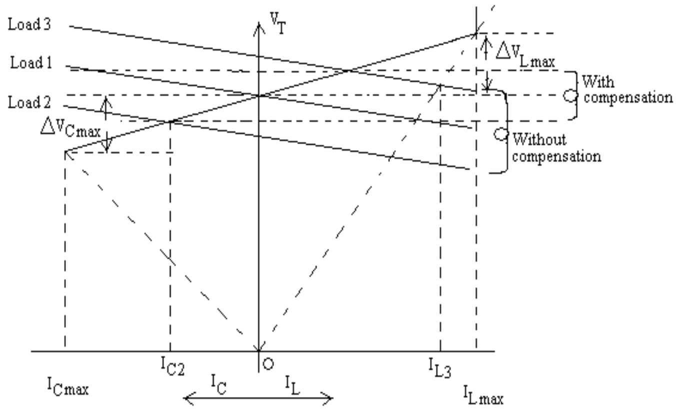

Fig.9. Dynamic V-I Characteristics of SVC with Load lines

V_{Cmax} = voltage limit of capacitor

B_C = admittance of capacitor

V_{Lmax} = voltage limit of TCR

I_{Cmax} = capacitive current limit

I_{Lmax} = inductive current limit

B_{Lmax} = max inductive admittance

III. FUZZY LOGIC CONTROLLER

Fuzzy logic is a new control approach with great potential for real time applications [2] [3]. Fig.10 shows the structure of the fuzzy logic controller (FIS-Fuzzy inference system) in MATLAB Fuzzy logic toolbox. [5][6].Load voltage and load current taken as input to fuzzy system. For a closed loop control, error input can be selected as current, voltage or impedance, according to control type [7]. To get the linearity triangular membership function is taken with 50% overlap. The output of fuzzy controller taken as the control signal and the pulse generator provides synchronous firing pulses to thyristors as shown in fig.11. The Fuzzy Logic is a rule based controller, where a set of rules represents a control decision mechanism to correct the effect of certain causes coming from power system [8] [9]. In fuzzy logic, the five linguistic variables expressed by fuzzy sets defined on their respective universes of discourse. Table-I shows the suggested membership function rules of FC-TCR controller. The rule of this table can be chosen based on practical experience and simulation results observed from the behavior of the system around its stable equilibrium points.

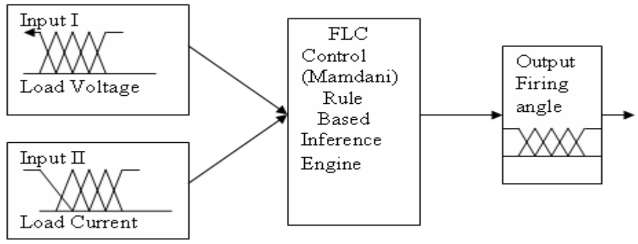

Fig.10. Structure of fuzzy logic controller

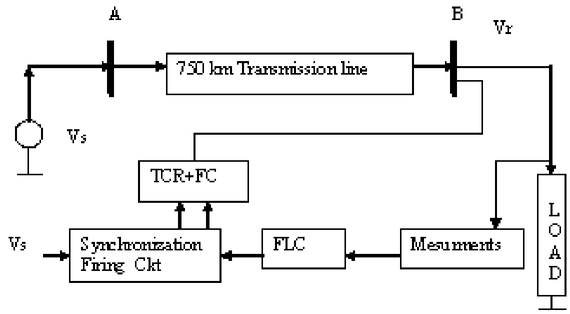

Fig.11. Single Phase equivalent circuit and fuzzy logic control structure of SVC

Table I. Membership function rules

		Load voltage				
		NL	NM	P	PM	PB
Load current	NL	PB	PB	NM	NM	NL
	NM	PB	PB	NM	P	NL
	P	P	PM	NM	NM	P
	PM	NM	P	NM	NM	PM
	PB	NL	NM	NM	NL	NL

IV. HARDWARE IMPLEMENTATION

An available simple two-bus artificial transmission ($\lambda/8$) line model of 4π line segments with 750 km, distributed parameters were used in this study. The line inductance 0.1mH /km, capacitance 0.01µf/km and the line resistance 0.001Ω were used. Each π section is of 187km, 187km, 188km and 188 km. Supply voltage is 230V - 50 Hz having source internal resistance of 1 Ω connected to node A. Static load is connected at receiving end B .The load resistance was varied to obtain the voltage variations at the receiving end. A shunt branch consisting of inductor and capacitor is added to compensate the reactive power of transmission line. With the change of load and due to Ferranti effect, the variations in voltages are observed at receiving end B of transmission line [9] [10]. The practical values of shunt elements are varied for different loading conditions to get both sending and receiving end voltages equal. As shown in Table II.

Table II compensated practical values of inductor and capacitor

S.NO	Load Resistance Ω	Compensating Inductance	Compensating Capacitance (µf)
1.	500	0.8 H	1
2.	400	0.9H	1
3.	300	0.19H	2
4.	200	0.18 H	5
5	150	0.19H	5
6	100	0.22H	8
7	50	0.14	8.5
8	40	0.14	9.0
9	30	0.14	10
10	20	0.14	12

A. FIRING CIRCUIT DESIGN

IC TCA 785 a 16 pin IC shown in Fig.12 is used in this study for firing the SCRs. This IC having output current of 250 mA and a fuzzy logic trainer kit with two input variables and having 5 linguistic sets is used. This can generate 5 X 5 rules. The output of fuzzy logic which varies from DC -10V to +10V is given to IC 785 controller pin11, which controls the comparator voltage VC ,and the firing angle α for one cycle and (180 +α) during negative cycle shown in fig.13

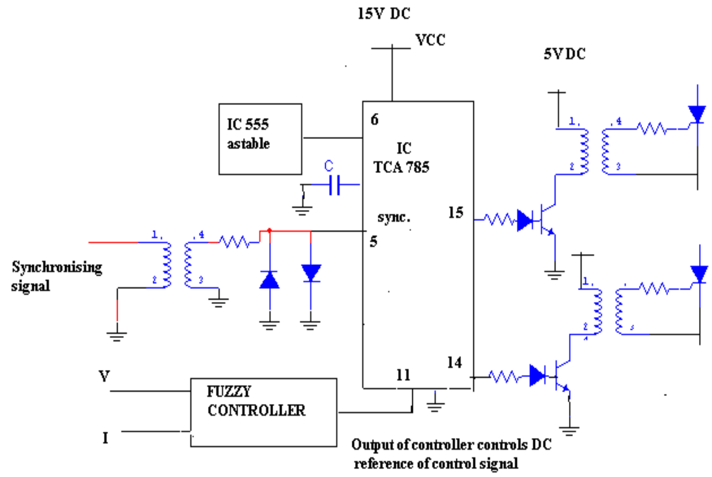

Fig.12. Firing Scheme with TCA 785 IC

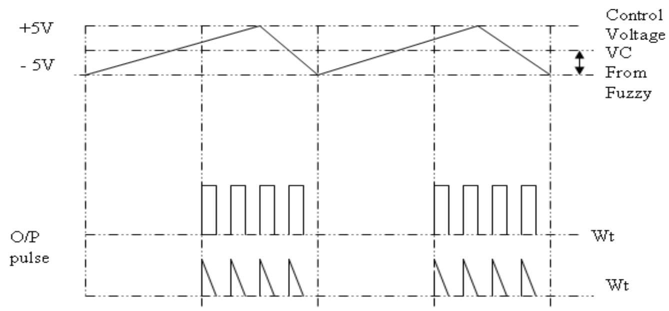

Fig.13.Generation of wave forms of TCA 785 IC

V. TEST RESULTS

The transmission line without any compensation was not satisfying the essential condition of maintaining the voltage within the reasonable limits. The effect of increasing load was to reduce the voltage level at the load end. At light loads, the load voltage is greater than the sending end voltage as the reactive power generated is greater than absorbed. At higher loads the load voltage drops, as the reactive power absorbed is greater than generated, as shown in Table III. Fig.14 and Fig.15 indicates unequal voltage profiles. Fig.16 clearly shows the firing angle and inductor current control.

Table III Load voltage before and after compensation

Tr Line Parameters for Lt=.10mh/km Ct =0.1μf/km R.= 0.001Ω		Before compensation For Vs= 230V (p-p)		After Compensation For L= 0.19H C= 8μ f For Vs= 230 (P-P)		
R Ω	V_S (rms) Volts	V_R (rms) Volts	I_R rms Amp	V_R (rms) Volts	I_R (rms) Amp	α.
500	162.6	270.80	0.54	162.1	2.032	90

400	162.6	268.10	0.67	162.4	2.036	100
300	162.6	268.00	0.89	162.	2.099	102
200	162.6	261.10	1.30	162.7	2.182	103
180	162.6	258.10	1.43	162.4	2.198	105
160	162.6	256.10	1.59	162.3	2.232	106
140	162.6	250.30	1.78	162.8	2.299	108
120	162.6	243.80	2.03	161.8	2.357	109
100	162.6	234.20	2.34	162.4	2.459	112
80	162.6	219.50	2.74	163.3	2.651	117
60	162.6	195.80	3.26	162.3	3.071	128
50	162.6	156.50	3.91	162.5	4.124	158

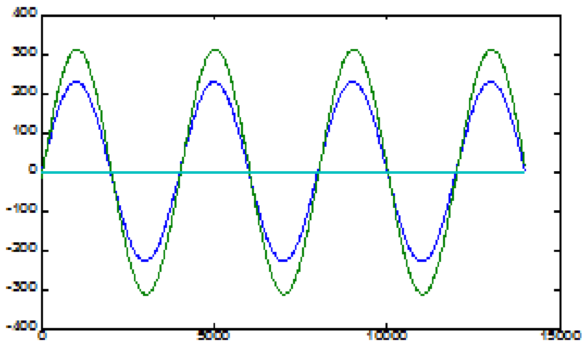

Fig.15. Uncompensated voltage for light load

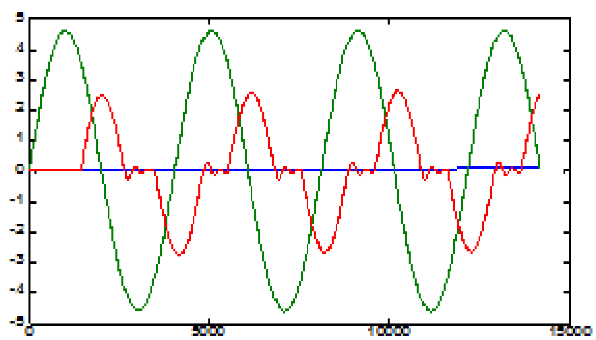

Fig.16. Inductor Current for firing angle 165 deg

VI. CONCLUSION

This paper presents an "online Fuzzy control scheme for SVC"and it can be concluded that the use of fuzzy controlled SVC (FC-TCR) compensating device with the firing angle control is continuous, effective and it is a simplest way of controlling the reactive power of transmission line. It is observed that SVC device was able to compensate both over and under voltages. Compensating voltages are shown in Fig.17 and Fig.18. The use of fuzzy logic has facilitated the closed loop control of system, by designing a set of rules, which decides the firing angle given to SVC to attain the required voltage. With MATLAB simulations [4] [5] and actual testing it is observed that SVC (FC-TCR) provides an effective reactive power control irrespective of load variations.

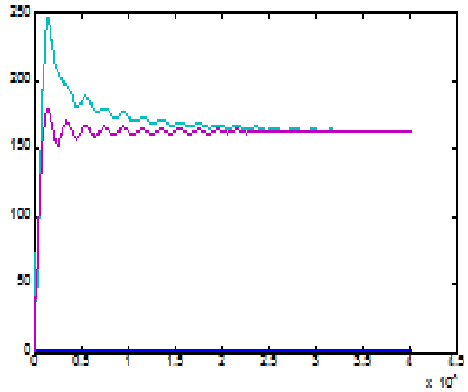

Fig.17. Compensated $V_R = V_S$ (RMS voltage) for R=200Ω

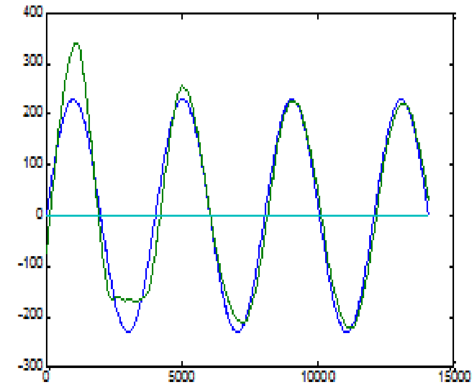

Fig.18. Compensated $V_R = V_S$ (instantaneous voltage) For R=200 Ω

VII. REFERENCES

[1] Narain. G. Hingorani, "Understanding FACTS, Concepts and Technology Of flexible AC Transmission Systems", by IEEE Press USA.

[2] Bart Kosko, "Neural Networks and Fuzzy Systems A Dynamical Systems Approach to Machine Intelligence", Prentice-Hall of India New Delhi, June 1994.

[3] Timothy J Ross, "Fuzzy Logic with Engineering Applications", McGraw-Hill, Inc, New York, 1997.

[4] Laboratory Manual for Transmission line and fuzzy Trainer Kit Of Electrical Engineering Department NIT Warangal

[5] SIM Power System User Guide Version 4 MATLAB Manual

[6] Periodicals and Conference Proceedings:

[7] S.M.Sadeghzadeh M. Ehsan " Improvement of Transient Stability Limit in Power System Transmission Lines Using Fuzzy Control of FACTS Devices ,IEEE Transactions on Power System Vol.13 No.3 ,August 1998

[8] Chuen Chien Lee "Fuzzy Logic in Control Systems: Fuzzy Logic Controller". Part I and Part II. IEEE R. IEEE transactions on system, man ,and cybernetics ,vol.20 March/April11990

[9] A.M. Kulkarni, "Design of power system stabilizer for single-machine system using robust periodic output feedback controller", IEE Proceedings Part – C, Vol. 150, No. 2, pp. 211 – 216, March 2003. Technical Reports: Papers from Conference Proceedings unpublished):

[10] U.Yolac,T.Talcinoz Dept. of Electronic Eng.Nigde 51200,Turkey "Comparison Compariiison of Fuzzy Logic and PID Controls For TCSC Using MATLAB"

[11] Jaun Dixon ,Luis Moran, Jose Rodrfguz ,Ricardo Domke "Reactive power compensation technology state- of-art- review"(invited paper) Electrical Engineering Dept Pontifica Universidad Catolica De CHILE.

IMAGE ENHANCEMENT BASED ON COLOR RESTORATION TECHNIQUE

Bhargavi.V[1], Swetha.P[2]

[1]Department of ECE, Mallareddy college of Engineering& Technology, Hyderabad, (India)

[2]Associate Professor Department of ECE, Mallareddy college of Engineering& Technology, Hyderabad, (India)

ABSTRACT

The paper presents the color image enhancement based on restore techniques. In this work, we propose two color restoration techniques are used. They are multi-scale technique and adaptive filter technique. In multi-scale retinex is to enhance the quality of the image and achieve color constancy. It suffers the color and halo distortion. The adaptive filter finds the importance of color information in color image enhancement and obtains better visibility. It reduces the halo and color distortion. The experimental results shows the adaptive filter is better performance compare to multi-scale retinex.

Index Term: - Adaptive Filter, Color Image Enhancement, Color Space Conversion and Retinex Human Visual System,

I.INTRODUCTION

Standard image enhancement techniques modify the image by using techniques such as histogram equalization, specification etc. [1] so that the enhanced image is more pleasing to the visual system of the user than the original image. Retinex [2-3] is an effective technique for color image enhancement, which can produce a very good enhanced result. But the enhanced image has color distortion and the calculation is complex. Li Tao and Vijayan K. Asari proposed a robust color image enhancement algorithm [4]. The algorithm can enhance color image without distortion, but the edges of the color image could not be handled well. The algorithm use Gaussian filter to estimate background image. Gaussian kernel function is isotropic, which leads to the inaccurate estimation of background image, resulting in the halo phenomenon. Considering the above two algorithms, a new bio-inspired color image enhancement algorithm is proposed by the author [5]. The algorithm is based on bilateral filter and has much better effect than the above mentioned two algorithms. However, the image still exhibits halo phenomenon at the edges in spite of the algorithm improving it. In [5], distance and luminance information of pixels are considered in the bilateral filter instead of only considering distance information in Gaussian filter. But the color information is still not taken into consideration. Another scheme, named Recursive Mean-Separate Histogram Equalization (RMSHE), has been proposed to preserve the brightness [6]. RMSHE uses the BBHE iteratively. First RMSHE separates the input histogram into two pieces, by the mean. Then, to each piece, it uses this operation many times to generate 2n-pieces histograms. Finally, it equalizes each histogram piece independently. It is claimed theoretically that when the iteration level n grows larger, the output mean converges to the input mean, and thus yields good brightness preservation. Actually, when n grows to infinite, the output histogram is exactly the input histogram, and thus the input image will be output without any enhancement at all. In this paper is organized as follows. Modified Multi-scale retinex method in section II. Explain the adaptive filter in section III. Measures are present in section IV. The simulation results are presented in Section V. Concluding remarks are made in section VI.

II. MODIFIED MULTI-SCALE RETINEX (MSR)

Multi-scale retinex technique is a color restoration technique that convolution of surrounding function (F(x,y)) into image distribution and then subtraction the image distribution is given by

$$R_i(x,y) = \log I_i(x,y) - \log [F(x,y) * I_i(x,y)] \quad (1)$$

Where RI(x, y) is the single scale retinex of ith color. Ii is the image distribution. F is the Gaussian surrounds function and is given by

$$F(x,y) = K e^{\frac{-r^2}{c^2}} \quad (2)$$

Where c is the Gaussian surround space constant and K is selected such that

$$\iint F(x,y)\,dx\,dy = 1 \quad (3)$$

The multi scale retinex is simply multiply the weighted sum with several R is given by

$$R_{MSR\,I} = \sum_{n=1}^{N} W_n R_{ni} \quad (4)$$

Where N is the number of scales, Rni is the ith color of the nth scale, R_{MSRi} is the ith color component of the MSR output, and wn is the weight associated with the nth scale. The color restoration method for the MSR is given by

$$C_i(x,y) = \log [\alpha\, I_i(x,y)] - \log \left[\sum_{i=1}^{S} I_i(x,y)\right] \quad (5)$$

Where α is a constant parameter of the color restoration function.

The block diagram of MSR is given by

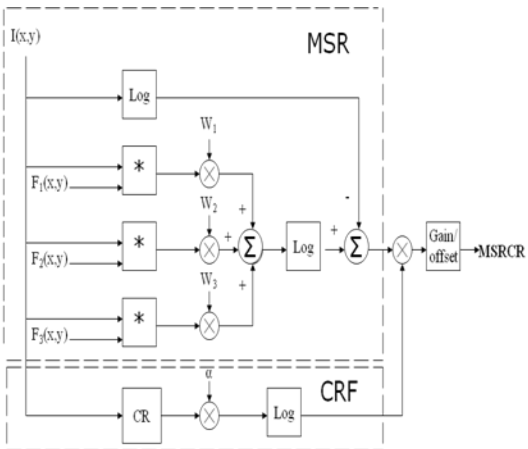

Fig.1. The Block Diagram Of MSR

After performing MSR on that image, the histogram of the Ri image was plotted and find the variance found from that. The clipping point was taken as 'y' times the variance where 'x' can take from 1 to 3 in any image.

This y value cannot work for all images. So to avoid that problem using frequency of occurrence of pixels in the histogram as a control measure. The clipping point was chosen as y=0.005, to get the better enhancement in all images. The MSR is a suffers a halo distortion and less contrast enhancement.

III. ADAPTIVE FILTER

This technique is solving the halo distortion and better enhancement compare to MSR. It consists of three major parts. 1) Luminance image and background image 2) adaptive adjustment and 3) color restoration.

The block diagram of adaptive filter is given by

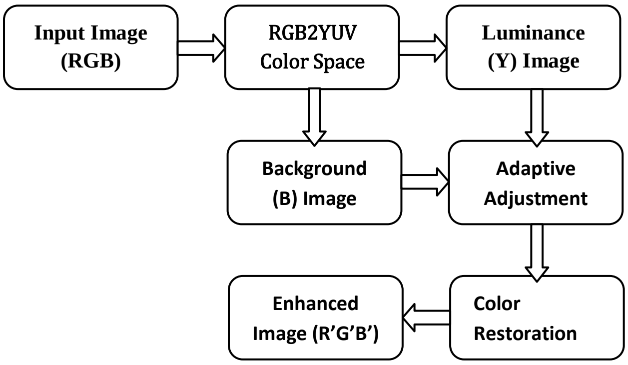

Fig.2. Block Diagram of Adaptive Filter

Firstly, convert the color image to YUV color space. Y stands for the luminance, and U, V are color components, which constitute the color information of RGB image. The luminance is the logarithmic function is expressed as

$$I_L(x,y)=\log(Y(x,y))/\log(\text{range}) \quad (6)$$

Where range is the highest pixel value i.e range=255.

Secondly, calculate the background image whose pixels are decided by the distance. The background image I_B of Y,U,V color image is given by

$$I_B(x,y) = \frac{\sum G_R G_N N(x,y)}{\sum G_R G_N} \quad (7)$$

Where

The N(x,y) represents the pixel of (x,y).

G_N is the scale parameter of pixel filtering

G_R is the distance parameter of intensity image. We use the below formula to obtain the distance parameter

$$G_R(x,y,x_i,y_j) = \exp\{-\frac{(x-xi)2+(y-yi)2}{2\sigma_N^2}\} \quad (8)$$

G_I is the distance parameter of U,V image is given by

$$G_I(x,y,x_i,y_j) = \exp\{\frac{(I(x,y)-I(xi,yj)}{2\sigma_i^2} \quad (9)$$

Gc is the scale parameter of U,V is given by

$$G_C(x,y,x_i,y_j) = \exp\{\frac{(U(x,y)-U(xi,yj)2+(V(x,y)-V(xi,yj)2}{2\sigma_C^2}\} \quad (10)$$

HereU(x,y),V(x,y) = chrome images of YUV image

I(x,y)=intensity value at (x,y) σ_R ,σ_I ,σ_C are the scale parameters, whose values are 20,30 ,60 respectively.

Thirdly, calculate the adaptive adjustment is given by

$$I_E(x,y)=\beta(x,y).I_L(x,y) \tag{11}$$

Where β(x,y) is the pixel coefficients and I_L is the luminance image.

After adaptive adjustment, apply the index transform of IE and restoration to get the color enhancement image. The adaptive filter technique is solving the halo distortion, color distortion compare to multi-scale retinex. It has less complexity and computation time.

IV. ENHANCEMENT MEASURE

In this work, we consider two enhancement measurements. They are entropy and brightness error. The entropy is calculated as

$$\text{Entropy} = -\sum_i P_i \log_2 P_i \tag{12}$$

In the above expression, P_i is the probability that the difference between 2 adjacent pixels is equal to i. If entropy is high to get the better enhancement.

The brightness error (AMBE) is calculated as

$$AMBE(X, R)=|E(X)-E(R)| \tag{13}$$

Where E (.) denotes the expectation (i.e., mean), R is the referenced image, and here R represents the original image.

The mean brightness and entropy are computed and listed in Table I.

image	entropy	AMBE
person	6.75	0.023
lena	6.23	0.016

Table 1. Entropy and AMBE of Results Image

V. EXPERIMENTAL RESULTS

These work simulated using MATLAB TOOL. In this work, to show the adaptive filter and modified filter technique results.

Fig.3. Person Image

Fig.4. Image Enhancement Based on Modified Multi Scale Retinex

Fig.5. Image Enhancement Based On Adaptive Filter

VI. CONCLUSION

In this work, presents the color image enhancement based on adaptive filter and modified multi scale retinex. The adaptive filter is solving the halo distortion, color distortion compare to multi-scale retinex. It has less complexity and computation time.The result show the better performance of adaptive filter compare to modified multi scale retinex.

REFERENCES

[1] R. C. Gonzalez, R. E. Woods, "Digital Image Processing," Third Edition, Pearson Publications.

[2] Funt B, Ciurea F, McCann J. Retinex in MATLAB[J]. Journal of Electronic Imaging, 2004, 13(1): 48-57.

[3] Kimmel R, Elad M, Shaked D, et al. A variational framework for Retinex [J]. International Journal of Computer Vision, 2003, 52(1): 7-23.

[4] Li Tao, Vijayan K... Asari. A Robbust Image Enhancement Technique for Improving Image Visual Quality in Shadowed Scenes[A]. Proccedings of the 4th International Conference on Image and Video Retrieval[C]. Springer, Berlin, ALLEMAGNE,2005, vol.3568,395-404.

[5] Wang Shou-jue, Ding Xing-hao, Liao Ying-hao, Guo dong-hui, A Novel Bio-inspired Algorithm for Color Image Enhancement, Acta Electronica Sinica, 2008.10, Vol.36, No.10: 1970-1973.(in Chinese)

MATERIALS FOR ADVANCED FUSION AND FISSION REACTORS

Mayank Khandelwal[1], Pranav Ravi[2], Nikita Agarwal[3]
[1, 2, 3] Department of Manufacturing Technology, JSSATE, Noida, Uttar Pradesh, (India)

ABSTRACT

Structural materials represent the key for containment of nuclear fuel and fission products as well as reliable and thermodynamically efficient production of electrical energy from nuclear reactors. Similarly, high-performance structural materials will be critical for the future success of proposed fusion energy reactors, which will subject the structures to unprecedented fluxes of high-energy neutrons along with intense thermo-mechanical stresses. Advanced materials can enable improved reactor performance via increased safety margins and design flexibility, in particular by providing increased strength, thermal creep resistance and superior corrosion and neutron radiation damage resistance. In many cases, a key strategy for designing high-performance radiation-resistant materials is based on the introduction of a high, uniform density of nano-scale particles that simultaneously provide good high temperature strength and neutron radiation damage resistance.

Keywords: Corrosion, Fission, Fusion, Nano-Scale Particles, Neutrons, Radiation

I. INTRODUCTION

Advanced Nuclear Materials discusses the major classes of materials suitable for usage in nuclear fission, fusion reactors and high power accelerators, and for diverse functions in fuels. The work addresses the full panorama of contemporary international research in nuclear materials, from Actinides to Zirconium alloys. Considerable changes in the operating performance of fission reactors, along with advances in the plasma physics knowledge required for heating and controlling fusion energy reactions suggest that fission and fusion energy can be important components of the overall energy portfolio for the 21st century and beyond. Advanced materials can enable improved reactor performance via increased safety margins and design flexibility, in particular by providing increased strength, thermal creep resistance and superior corrosion and neutron radiation damage resistance.

II. FISSION

A power reactor core contains fuel rods with a height of ~4 m and diameter ~1 cm. As illustrated in Fig. 1, a wide range of structural materials are used for a diverse variety of roles in fission reactors. The fuel cladding serves to reliably contain the fuel and radioactive fission products while efficiently transferring the intense nuclear heat from the fuel to the coolant. The typical heat flux through the cladding is ~1 MW/m^2 (~1% of the heat flux at the surface of the sun). Zirconium alloys are used as fuel cladding in most commercial reactors, due to their compatibility with $UO_2$and water, their adequate thermal conductivity and ease of manufacturing. A large number of these reactors are based on uranium dioxide fuel pellets arranged in long cylinders ("fuel rods") with surrounding flowing water channels.

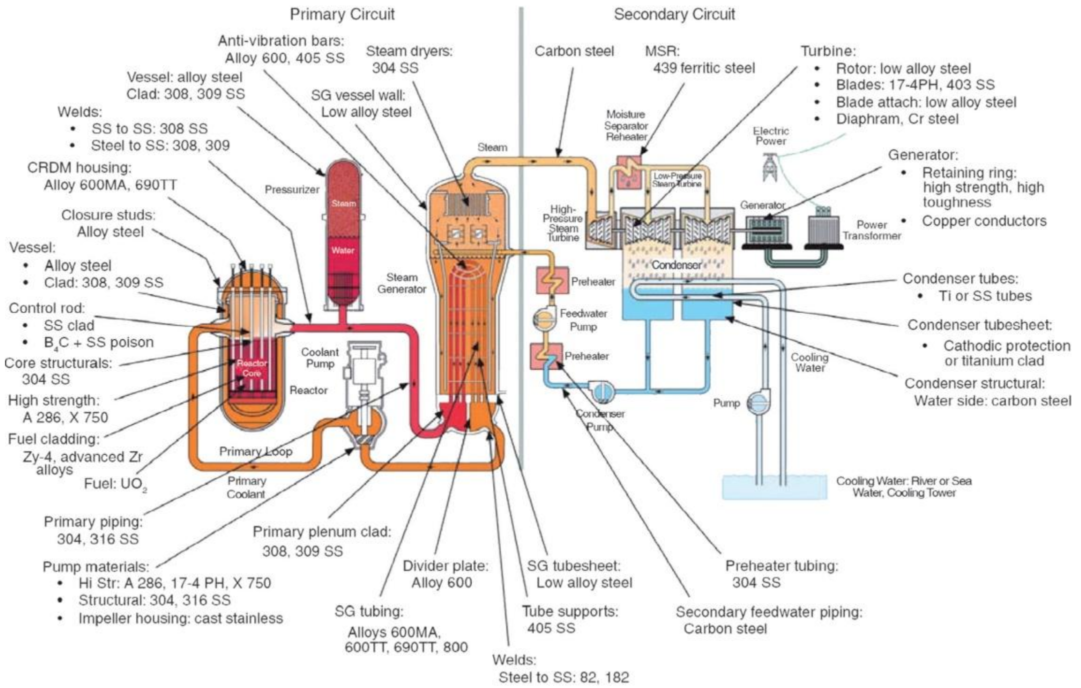

Fig.1: Diverse range of structural materials used in fission reactors

The fuel remains in the reactor for several years, with the cladding being subjected to high temperatures (3500C-4000C), mechanical stress, and intense radiation. Main problem includes oxidation, hydriding, build-up of low thermal conductivity corrosion deposits, and effect of hydrogen on cracking and corrosion. These core internal structures must reliably operate for over 30 years in a high radiation environment (resulting in higher accumulated doses than the fuel cladding in many cases) at ∼300 °C without substantial dimensional changes or degradation in mechanical properties due to stress corrosion cracking or radiation damage. The reactor pressure vessel (quenched and tempered Mn-Mo-Ni low-alloy pressure vessel steel) serves as the critical safety boundary between the reactor and the environment, and is generally considered the key lifetime-limiting (irreplaceable) component for a nuclear reactor. Major concern is loss of fracture toughness due to radiation-induced defect cluster hardening and radiation-induced precipitation. The embrittlement is monitored by regular mechanical property testing of specimens located at the inside wall of the pressure vessel. Piping and heat exchanger materials (ferritic steels and Ni-base alloys such as Alloy 600 and 690) are designed to enable reliable and thermodynamically efficient conversion of thermal energy from the reactor into steam that drives turbines to generate electricity. Due to desire for reliable operation for decades at elevated temperatures in an aqueous environment at 300 to 350 °C, main concerns for the piping and heat exchanger materials include thermal aging and complex water chemistry issues that may induce corrosion or stress corrosion cracking. Aqueous corrosion is a complex form of degradation that is dependent on temperature, material condition, material composition, water purity, water pH, water impurities, and dissolved gas concentrations. The predominant corrosion mechanism varies with location in the reactor core and multiple mechanisms may be simultaneously operating[1 and 2]

III. FUSION

Continuous advancement over several decades has taken fusion researchers to the brink of demonstrating the plasma physics feasibility of fusion energy via magnetically-confined and inertially confined concepts. A schematic of a prototypic magnetic fusion energy reactor is shown in Fig.2. The fusion reactions are induced within a toroidal-shaped high temperature ionized plasma that is shaped by powerful toroidal and poloidal field magnets. The heat and energetic neutrons produced by the deuterium-tritium (D-T) fusion reaction are absorbed by the surrounding first wall, blanket, and divertor components. The fusion reaction occurs inside a vacuum vessel to prevent atmospheric contamination of the D-T plasma. The major functions of the blanket region are to efficiently capture the energy produced by the fusion reactions and transfer the heat to a coolant for electricity generation, and to create and extract fresh tritium fuel (by utilizing nuclear transmutation reactions with lithium-containing liquid or solid materials) to enable continuous operation of the fusion energy system. A wide variety of structural materials, reactor coolants, and tritium generation materials systems have been evaluated for potential use in future fusion reactors. Table 1 summarizes the material combinations that are considered to be the most promising based on thermodynamic efficiency, neutronics, chemical compatibility, and other engineering considerations

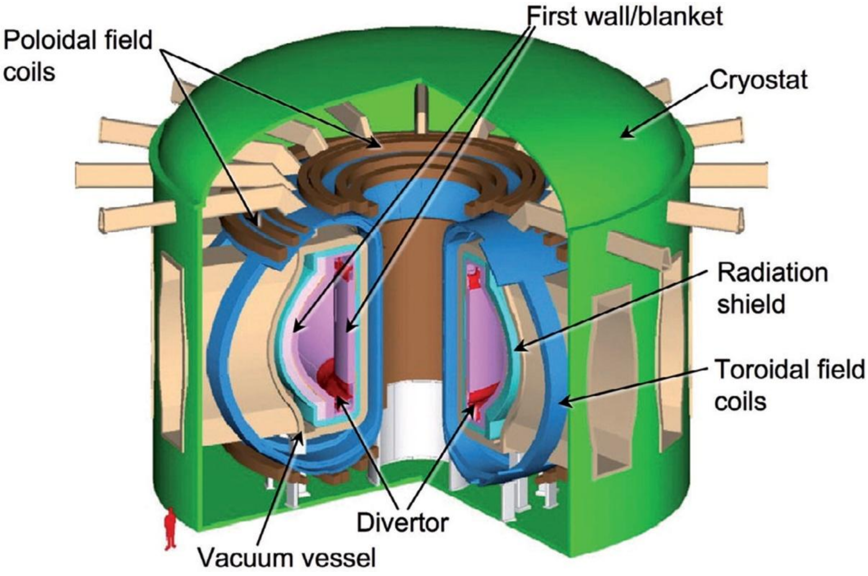

Fig.2: Schematic Diagram of Fusion Reactor

material	Li/Li	He/PbLi	He/Li Ceramic	FLiBE
Ferritic steel			✓	
V alloy		✓		✓
SiC/SiC				✓

TABLE 1.

Summary of leading proposed structural materials, coolant and tritium generation concepts for fusion energy systems [3 and 4]. The filled cells in the table indicate material combinations that are under consideration for fusion energy blankets. FLiBe is a LiF- BeF_2molten salt.

High-performance structural materials will be critical for the future success of proposed fusion energy reactors, which will subject the structures to unprecedented fluxes of high-energy neutrons along with intense thermo-mechanical stresses and high temperature coolants that may induce corrosion [3, 6, 7, 9,10]. The high average neutron energy associated with the deuterium-tritium fusion reaction compared to fission tends to produce much higher levels of transmutant solutes such as H and He in the structural materials that generally magnify radiation-induced degradation processes. Consideration of this reduced-activation mandate, along with the requirement for high performance, leads to three major options for fusion structural materials. Ferritic/martensitic steel (where high activation solutes such as Mo and Nb in commercial steels are replaced by W and V) is the most mature option[5,10,11,12,] Oxide dispersion strengthened steel represents a promising future higher-performance option if non-uniformity, joining, and high cost can be resolved. Refractory alloys based on either vanadium or tungsten alloys represent a higher performance, higher risk option. Vanadium alloys are preferred for self-cooled lithium blanket systems, but are not effective with other blanket concepts[5]. SiC/SiC ceramic composites offer the potential for the highest thermodynamic efficiency and best safety and waste disposal margins, but are least developed for large-scale structural applications.

IV. RADIATION DAMAGE

The kinetic energy of the neutrons produced by the fission and fusion reactions is sufficient to dislodge substantial numbers of atoms in structural materials from their lattice sites over the projected operating lifetimes of the reactors, creating defects associated with the missing lattice atoms (vacancies) and the dislodged atoms that reside in the lattice interstices (self-interstitial atoms, SIAs). The amount of radiation damage from these ballistic collisions is quantified in terms of displacements per atom (dpa). A damage level of 1 dpa corresponds to “stable” displacement of every atom from its lattice site. For reactor operating temperatures, there is sufficient thermally activated diffusion of the radiation-induced defects to enable recombination of many of the vacancies and SIAs so that the retained displacement damage is a fraction of the dpa value. An important strategy for designing radiation resistant materials is to promote very efficient recovery of the defects: Very little can be done to alter the instantaneous displacement damage from exposure to energetic neutrons, but substantial resistance to radiation damage can be engineered by efficiently facilitating the recombination of these defects. Considering that dimensional instabilities above a few percent generally cannot be tolerated in large-scale engineering structures and that future reactor designs call for structural materials that will be exposed to damage levels in excess of 100 dpa, the challenge is to develop materials with “self-healing” defect recombinations. It is a challenge that engineered defect recombination structures must be resistant to the vigorous transient (~1 fs to 1 ps) atomic mixing that occurs within fast neutron-induced displacement cascades; the magnitude of this transient atomic mixing is roughly two orders of magnitude higher than the dpa value[16,18,19] and could result in dispersal or dissolution of nano-scale precipitate structures. Radiation damage poses five main threats to the operation of structural materials, emerging at different operating temperatures and damage levels. These phenomena are summarized in Fig.3. At low temperatures (below 0.3–0.4 TM, where TM is the absolute melting temperature), radiation-induced defect clusters (predominantly created directly in displacement cascades) serve as strong obstacles to dislocation motion. This radiation hardening is usually accompanied by substantial reductions in uniform elongation and macroscopic work hardening capacity, and can induce loss of fracture toughness in body centered cubic metals and alloys. Since the radiation hardening emerges at relatively low doses (0.001 to 0.1 dpa), radiation hardening and embrittlement often defines the lower operating temperature limit for structural materials in neutron irradiation environments. At intermediate temperatures, three distinct radiation effects phenomena are of potential significance for doses above ∼1 to 10 dpa: radiation-induced segregation and precipitation (0.3–0.6 TM) that can lead to localized corrosion or mechanical property degradation such as grain boundary embrittlement, void swelling from vacancy accumulation (0.3–0.6 TM) that can create unacceptable volumetric expansion, and radiation induced creep and/or anisotropic growth (0.2–0.6 TM) that can produce dimensional expansion along directions of high stress and/or specific crystallographic directions. At very high temperatures (>0.5 TM) and under applied mechanical stress, helium produced by neutron transmutation reactions in the structural material may migrate to grain boundaries and form cavities, thereby causing inter-granular fracture with limited ductility in stressed materials. This high temperature helium embrittlement of grain boundaries typically emerges for helium concentrations above 10 to 100 appm (∼1 to 100 dpa depending on material and neutron spectrum) and becomes increasingly severe with increasing temperature and applied stress and decreasing deformation rate. Along with chemical compatibility and thermal creep strength, high temperature helium embrittlement may define the maximum allowable operating temperature for a structural material in neutron irradiation environments.

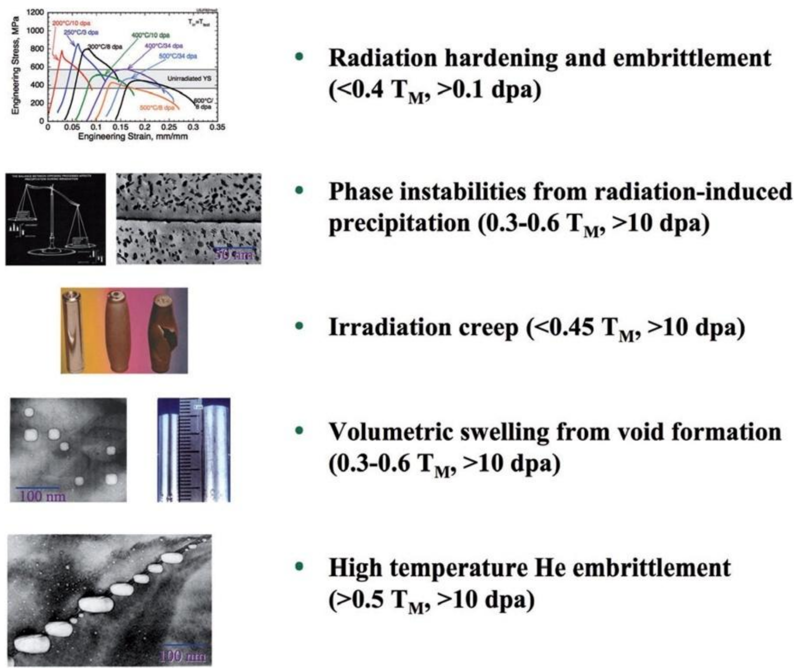

Fig.3: Threats to Operation Of Structural Materials

V. METHODS TO ENHANCE STRUCTURAL MATERIAL PROPERTIES FOR FUSION AND FISSION REACTORS

Known structural materials have limited operating temperature ranges where they can be utilized in a neutron irradiation environment [14] as summarized in Fig.4 for moderate damage levels of 10 to 50 dpa. At low temperatures, the low ductility associated with low temperature radiation hardening creates conditions where modified (larger safety margin) engineering design rules must be used. In cases where fracture toughness is reduced by low temperature irradiation, the operating temperature is restricted to higher temperatures where embrittlement does not occur for anticipated normal and transient operating conditions. The upper operating temperature limit is typically determined by thermal creep strength or high temperature helium embrittlement considerations. Advanced materials can enable improved reactor performance via increased safety margins and design flexibility, in particular by providing increased tensile strength, thermal creep resistance and superior neutron radiation damage resistance. A key strategy for designing high-performance radiation-resistant materials is based on the introduction of a high, uniform density of nano-scale particles that simultaneously serve as obstacles to dislocation motion (providing high strength) and point defect recombination centers (providing good radiation damage resistance)[13,15]. This shows that it may be possible to develop alloys with highly improved mechanical properties compared to conventional alloys by appropriate use of either evolutionary ingot-based steel metallurgy or alternative processing techniques such as powder metallurgy production of oxide dispersion strengthened steels. In either approach, development of a high density of thermally stable, nano-scale hardening centers produces good mechanical properties. The 14YWT nanocluster-strengthened alloy also exhibits very good high temperature particle stability and thermal creep strength, and has demonstrated good resistance to low-temperature neutron irradiation embrittlement in preliminary low-dose irradiation tests. Limited success has also been obtained in creating high strength structural alloys that simultaneously convey improved high temperature oxidation resistance.

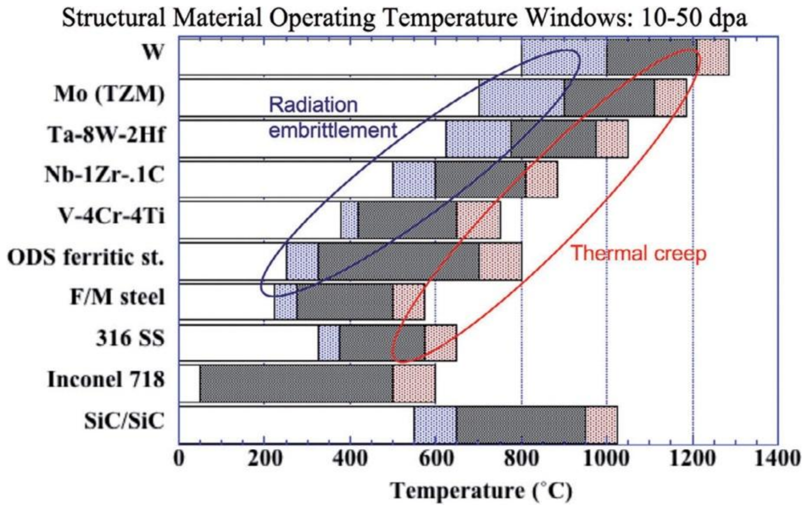

Fig.4: Materials Vs Temperature (Estimated Operating Temperature Windows {Dark Shaded Regions} For Structural Materials .The Light Blue and Red Regions Represent Lower and Upper Temperature)

Development of structural materials for large-scale energy application is a long and costly process, due to the extended period to develop a new alloy followed by an even longer proof testing period to validate the performance of the material in prototypic environments for appropriate licensing authorities. For example, Fig.5 shows the historical rate of progress in improving the upper operating temperature limit of steels for general (non-nuclear) structural applications has averaged ~2.5 °C/year for the past 60 years. Materials science tools such as computational thermodynamics and multi-scale radiation damage computational models, in conjunction with focused experimental validation studies (non-irradiation and irradiation environments), may offer the potential to reduce the time period to develop and qualify structural materials for advanced nuclear energy systems. It is seen that many structural materials currently being used in fission reactors are based on alloys that were originally developed in the 1950s and 1960s.

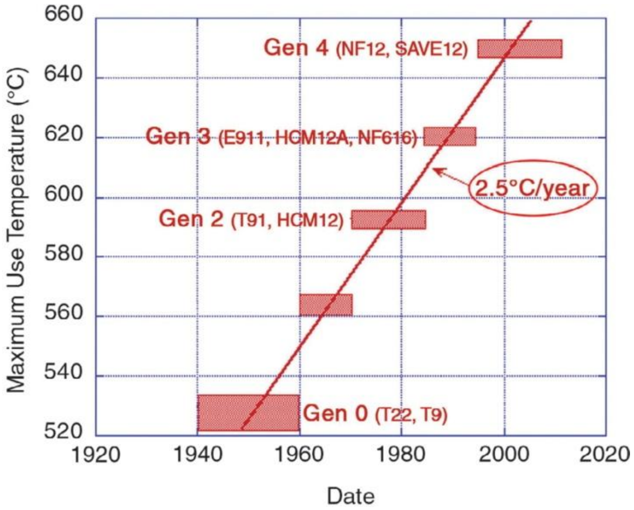

Fig.5 Upper Operating Temperature Limit Of Steels For General Structural Applications.

There are numerous examples where high-performance materials are being developed with the assistance of modern materials science tools [12, 13, 15]. For example, first principles atomistic modeling results provided important insight that the formation of highly stable nanoscale clusters enriched in Y, Ti and O from initial Y2O3 and Fe-Ti master alloy powders in a nanocluster-strengthened ferritic steel may have been enabled by the high concentration of vacancies produced during ball milling as part of the powder metallurgy processing of this steel. This nanocluster-strengthened ferritic steel has exhibited very high strength and good fracture toughness down to 120 K, and did not exhibit the sharp degradation in fracture toughness following neutron irradiation to moderate doses near 300 °C that caused embrittlement in conventional ferritic/martensitic steel. Similarly, ultra-high strength precipitation-hardened steels with adequate fracture toughness have recently been developed by carefully controlling the formation of fine-scale (Mo, Cr)2C precipitates Fig.6 compares the fracture toughness versus tensile strength behavior for the Aermet precipitation-strengthened steel and the 14YWT nanocluster-strengthened steel with the behavior for conventional bainitic and ferritic-martensitic steels. In all steels, the classic tradeoff between high strength and high toughness is evident. However, the critical tensile strength above which fracture toughness is reduced to low values is approximately 700 MPa in the conventional steels, whereas it is nearly 2000 MPa in the nanocluster-strengthened and fine-scale (Mo, Cr)2C strengthened steels.

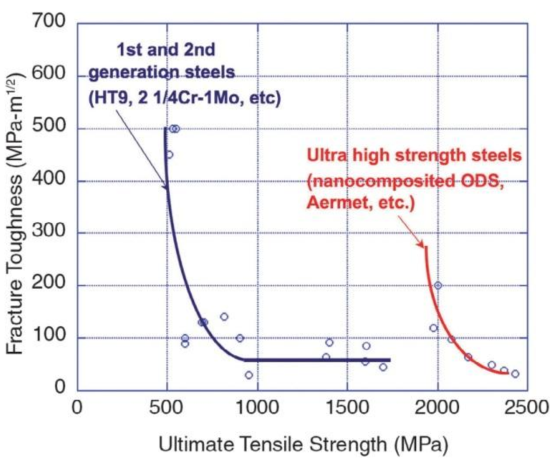

Fig.6 Fracture toughness versus Ultimate tensile strength

5.1 Future Fuel Concepts Under Consideration

UO_2 – Zircaloy (Base Case)

UO_2-FeCrAl(oxidation resistant Steel)

FCM-FeCrAl Fully Ceramic Microencapsulated Fuel

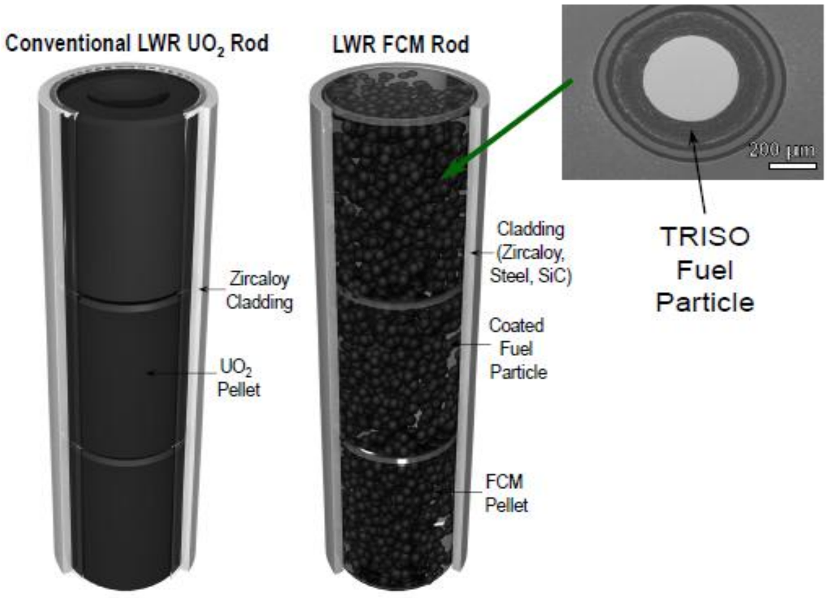

Fig.7: Cross-sectional view of fuel rod

VI. CONCLUSION

For fission and fusion energy systems to reach their full potential, high performance structural materials are needed that encompass improved mechanical strength, fracture toughness, good radiation resistance, and corrosion resistance. Development of a high density of uniformly distributed nanoscale hardening centers that are stable to thermal coarsening and radiation-induced growth or shrinkage is an attractive method to create a high-performance radiation resistant material. Emerging results from several classes of ferritic and austenitic steels suggest that substantial improvement in the performance of structural materials might be achievable. Considerable experimental validation will be needed to demonstrate the superior stability of these new alloys under prolonged exposure to high temperatures, mechanical stress, and neutron irradiation. Substantial improvement in the performance of structural materials can be achieved in a timely manner with a science-based approach like -Design of nanoscale features in structural materials confers improved mechanical strength and radiation resistance .Selection of accident-tolerant fuel options for light water fission reactors.

REFERENCES

[1] Was, G. S., Busby, J. T., and Andresen, P. L Corrosion Environments, 406.ASM Handbook, Vol. 13C, In Issue, 2006, 351-340.

[2] Goldston. R, Application of Nuclear Science, Journal of Fusion Energy, 2002, 21, 61.

[3] Moses, E. I, Physics of Nuclear Energy, Nuclear Fusion 49, article no. 104022, 2009, 22-27.

[4] Jacoby, M., Chemistry in the Nucleus, Chemical Engineering News, 87, 2009, 14.

[5] Zinkle, S. J., Fusion Engineering Design Handbook, 13, 2007, 31-32.

[6] Ehrlich, Nucleonic Matter Royal Society of London Article, 357, 1999, 595.

[7] Raj B, Rao KBS, Materials used in Nuclear Reactors, Journal of Nuclear Matter, 386, 2009,935.

[8] Pollard M, Processes to make Nuclear Materials, Journal of Advancement of Matter Processes, 161, 2003, 57.

[9] Sethian J. D, Fusion and its Principles, Fusion Science Technology Magazine, 56, 2009, 594.

[10] Holtkamp N, Materials and its properties, Fusion Engineering Journal, 84, 2009, 98.

[11] Olson G B, Science Research Magazine, 27, 1997, 1237.

[12] Boutard J L, Rendering Physics Book, 23, 1985, 567-590.

[13] S.J. Piet, E.T. Cheng, L.J. Porter Article of Fusion Technology, 17, 1990, 47.

[14] Gelles, D. S., In Reduced activation materials for fusion reactors, American Society for Testing and Materials: Philadelphia, 1990, 113.

[15] Klueh, R. L., Current Opinions in Solid State Materials Science, 8, 2004, 239.

Biographical Notes

Mr Mayank Khandelwal is presently pursuing B.Tech third year in Manufacturing Technology Department from JSS, Noida.

Mr. Pranav Ravi is presently pursuing B.Tech third year in Manufacturing Technology Department from JSS, Noida.

Mrs Nikita Agarwal is presently working as a Professor in Manufacturing Technology Department from JSS, Noida.

COMPARISON OF SLM & PTS TECHNIQUES FOR REDUCING PAPR IN OFDM

Bala Bhagya Sree. Ch[1], Aruna Kumari.S[2]

[1]*Department of ECE, Mallareddy college of Engineering& Technology, Hyderabad, India*
[2]*Associate Professor Department of ECE, Mallareddy college of Engineering& Technology, Hyderabad, India*

ABSTRACT

Orthogonal Frequency Division Multiplexing (OFDM) is an efficient method of data transmission for high speed communication systems. However, the main drawback of OFDM system is the high Peak to Average Power Ratio (PAPR) of the transmitted signals. OFDM consist of large number of independent subcarriers, as a result of which the amplitude of such a signal can have high peak values. Coding, phase rotation and clipping are among many PAPR reduction schemes that have been proposed to overcome this problem. Here two different PAPR reduction methods e.g. partial transmit sequence (PTS) and selective mapping (SLM) are used to reduce PAPR. Significant reduction in PAPR has been achieved using these techniques. The performances of the two methods are then compared.

Keywords-- ***Complementary Cumulative Distribution Function (CCDF) ,Orthogonal Frequency Division Multiplexing (OFDM), Peak-To-Average Power Ratio(PAPR),Partial Transmit Sequence (PTS), Quadrature Phase Shift Keying (QPSK), Selective Mapping (SLM)***

I. INTRODUCTION TO OFDM

Orthogonal frequency division multiplexing (OFDM) is a multicarrier modulation (MCM) technique which seems to be an attractive candidate for fourth generation (4G) wireless communication systems. OFDM offer high spectral efficiency, immune to the multipath delay, low inter-symbol interference (ISI), immunity to frequency selective fading and high power efficiency. Due to these merits OFDM is chosen as high data rate communication systems such as Digital Video Broadcasting (DVB) and based mobile worldwide interoperability for microwave access (mobile Wi-MAX). However OFDM system suffers from serious problem of high PAPR. In OFDM system output is superposition of multiple sub-carriers. In this case some instantaneous power output might increase greatly and become far higher than the mean power of system. To transmit signals with such high PAPR, it requires power amplifiers with very high power scope. These kinds of amplifiers are very expensive and have low efficiency-cost. If the peak power is too high, it could be out of the scope of the linear power amplifier. This gives rise to non-linear distortion which changes the superposition of the signal spectrum resulting in performance degradation. If no measure is taken to reduce the high PAPR, MIMO-OFDM system could face serious restriction for practical applications [1]-[4].

PAPR can be described by its complementary cumulative distribution function (CCDF). In this probabilistic approach certain schemes have been proposed by researchers. These include clipping, coding and signal scrambling techniques. Under the heading of signal scrambling techniques there are two schemes included. Which are Partial transmit sequence (PTS) and Selective Mapping (SLM). Although some techniques of PAPR reduction have been summarized in [5], it is still indeed needed to give a comprehensive review including some motivations of PAPR reductions, such as power saving, and to compare some typical methods of PAPR reduction through theoretical analysis and simulation results directly. An effective PAPR reduction technique should be given the best trade-off between the capacity of PAPR reduction and transmission power, data rate loss, implementation complexity and Bit-Error-Ratio (BER) performance etc.

II. OFDM PAPR DESCRIPTIONS

It is defined as the large variation or ratio between the average signal power and the maximum or minimum signal power Theoretically, large peaks in OFDM system can be expressed as Peak-to-Average Power Ratio (PAPR) and it is usually defined as [17]:

$$\text{PAPR} = \frac{P_{peak}}{P_{Average}} = 10\log_{10}\frac{\max\sqrt[2]{|X_n|}}{E\sqrt[2]{X[n]}} \qquad (1)$$

Where P_{peak} represents peak output power, Paverage means average output power. E[.] denotes the expected value, X_n represents the transmitted OFDM signals which are obtained by taking IFFT operation on modulated input symbols .Mathematical , is expressed as:

$$Xn = 1/N \sum_{k=0}^{N-1} X\, W_n^{nk} \qquad (2)$$

III. PAPR REDUCTION TECHNIQUES

Several PAPR reduction techniques have been proposed in the literature [6]. These techniques are divided into two groups - signal scrambling techniques and signal distortion techniques which are given below:

a) Signal Scrambling Techniques

- Block Coding Techniques
- Block Coding Scheme with Error Correction
- Selective Mapping (SLM)
- Partial Transmit Sequence (PTS)
- Interleaving Technique
- Tone Reservation (TR)
- Tone Injection (TI)

b) Signal Distortion Techniques

- Peak Windowing
- Envelope Scaling
- Peak Reduction Carrier
- Clipping and Filtering

One of the most pragmatic and easiest approaches is clipping and filtering which can snip the signal at the transmitter is to eliminate the appearance of high peaks above a certain level. But due to non-linear distortion introduced by this process, orthogonality [8] is destroyed to some extent which results in In-band noise and Out-band noise. In-band noise cannot be removed by filtering, it decreases the bit error rate (BER). Out-band noise reduces the bandwidth efficiency. but frequency domain filtering [7] can be employed to minimize the out-band power. Although filtering has a good effect on noise suppression, it may cause peak re-growth. To overcome this drawback, the whole process is repeated several times until a desired situation is achieved. Here, two signal scrambling techniques are used to overcome these problems.

3.1. Signal Scrambling Techniques

The fundamental principle of these techniques is to scramble each OFDM signal with different scrambling sequences and select one which has the smallest PAPR value for transmission. Apparently, this technique does not guarantee reduction of PAPR value below to a certain threshold, but it can reduce the appearance probability of high PAPR to a great extent. This type of approach include: Selective Mapping (SLM) and Partial Transmit Sequences (PTS). SLM method applies scrambling rotation to all sub-carriers independently while PTS method only takes scrambling to part of the sub-carriers.

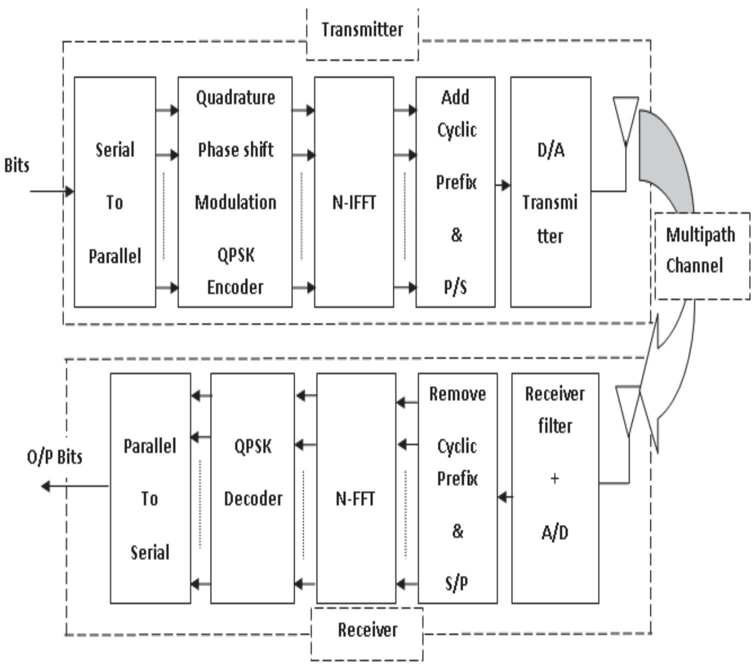

Fig.1 Block diagram of OFDM System

3.1.1 Selection Mapping Technique (SLM)

The CCDF of the original signal sequence PAPR above threshold PAPR0 is written as $Pr\{PAPR > PAPR0\}$. Thus for K statistical independent signal waveforms, CCDF can be written as $Pr\{PAPR > PAPR0\}^K$, so the probability of PAPR exceed the same threshold. The probability of PAPR larger than a threshold Z can be written as

$$\mathbf{P(PAPR < z) = F(z)^N = (1 - e^{-z})^N} \qquad \mathbf{(3)}$$

Assuming that M-OFDM symbols carry the same information and that they are statistically independent of each other. In this case, the probability of PAPR greater than Z is equals to the product of each independent probability. This process can be written as

$$\mathbf{P(\{PAPR_{low} > Z\}) = (P\{PAPR > Z\})^M = ((1e^Z)^N)^M} \quad \mathbf{(4)}$$

In selection mapping method, firstly M statistically independent sequences which represent the same information are generated, and next, the resulting M statistically independent data blocks Sm = [Sm,0,Sm,1,…….,Sm,N-1]T, for m=1,2,...,M are then forwarded into IFFT operation simultaneously. $X_{M=}$ [X1 , X2,…..,XM] in discrete time-domain are acquired and then the PAPR of these M vectors are calculated separately. Eventually, the sequences Xd with the smallest PAPR is selected for final serial transmission. Figure 1 shows the basic block diagram of selective mapping technique for suppressing the high PAPR.

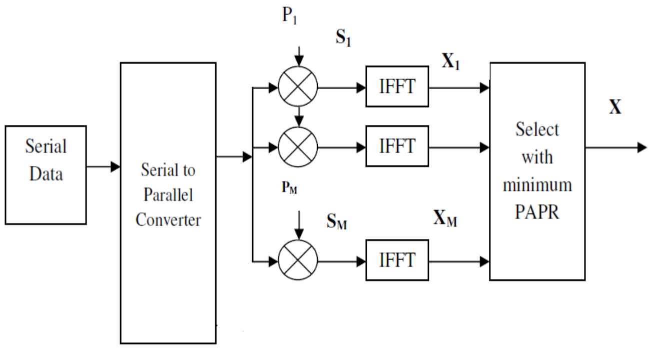

Fig.2 Bloch diagram of selective mapping

3.1.2 Partial Transmit Sequence

Partial Transmit Sequence (PTS) algorithm is a technique for improving the statistics of a multicarrier signal.The basic idea of partial transmit sequences algorithm is to divide the original OFDM sequence [9] into several sub-sequences and for each sub-sequences multiplied by different weights until an optimum value is chosen.

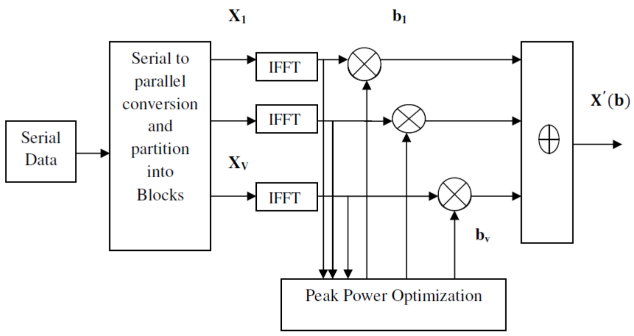

Figure 3. The Block diagram of PTS Technique

Figure 3 [10] is the block diagram of PTS technique. From the left side of diagram, the data information in frequency domain X is separated into V non-overlapping sub-blocks and each subblock vectors has the same size N. So for each and every sub-block it contains N/V nonzero elements and set the rest part to zero. Assume that these sub-blocks have the same size and no gap between each other. The sub-block vector is given by

$$X = \sum_{v=1}^{V} bvXv \quad (5)$$

where $bv = ej\emptyset v\,(\emptyset v \in [0,2\pi])\{v = 1,2, \dots \dots Xv\}$ is a weighting factor been used for phase rotation.

The signal in time domain is obtained by applying IFFT operation [11] on, that is

$$x = IFFT(X) = \sum_{v=1}^{v} bv\ IFFT(Xv) = \sum_{v=1}^{v} bv\ Xv \quad (6)$$

For the optimum result one of the suitable factor from combination b = [b1, b2,.., bv] is selected and the combination is given by

$$b = [b1,b2,\dots\dots,bv] = \mathrm{argmin}(b1,b2,\dots.bv)(\max 1 \le n \le N \left| \sum_{v=1}^{v} b\,vXv \right|^{2} \quad (7)$$

where arg min [(·)] is the condition that minimize the output value of function.

IV. REDUCTION OF PAPR

SLM and PTS algorithms are two typical non-distortion techniques for reduction of PAPR in OFDM system [12]-[16]. SLM method [15] applies scrambling rotation to all sub-carriers independently while PTS methods [16] only take scrambling to part of the sub-carrier.

Table 1 Parameters used in SLM and PTS algorithm

Parameters	Values used
Number of sub-carriers (N)	64, 128
Oversampling factor (OF)	8
Modulation scheme	QPSK
Route numbers used in SLM method (M)	2, 4, 8, 16
Number of sub-blocks used in PTS methods (V)	4
Total number of combinations or IFFT for weighting factor 1 and 2	16, 256

Table 1 show the parameters of OFDM signal which is used for PAPR reduction. Here, the number of sub-carriers used are N=64, 128 and the pseudo-random partition scheme is applied for each carrier, adopting QPSK constellation mapping, weighting factor being bv ∈ [±1,±j].

V. SIMULATION RESULTS

Figure 4 shows the CCDF as a function of PAPR distribution when SLM method is used with 64 numbers of subcarrier. Figure 5 shows the same result for 128 numbers of subcarrier. M takes the value of 1 (without adopting SLM method), 2, 4, 8 and 16. It is seen in Figure 4 and Figure 5 that with increase of branch number M, PAPR's CCDF gets smaller.

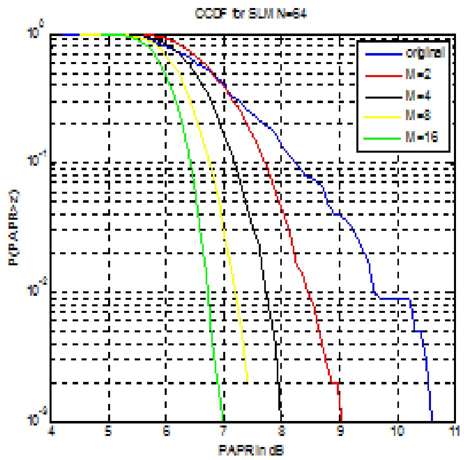

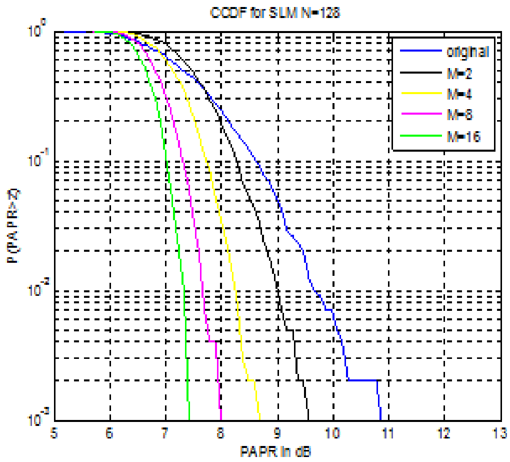

Figure 4. PAPR's CCDF using SLM method with N=64 **Figure 5. PAPR's CCDF using SLM method with N=128**

Now discussed the simulation result for PTS technique, there are varying parameters which impact the PAPR reduction performance these are: 1) The number of sub-blocks V, which influences the complexity strongly; 2) The number of possible phase value W, which impacts the complexity; and 3) The sub-block partition schemes. Here, only one parameter is considered that is sub-block size V.

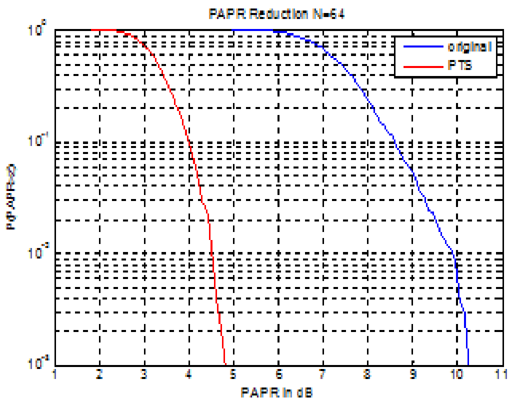

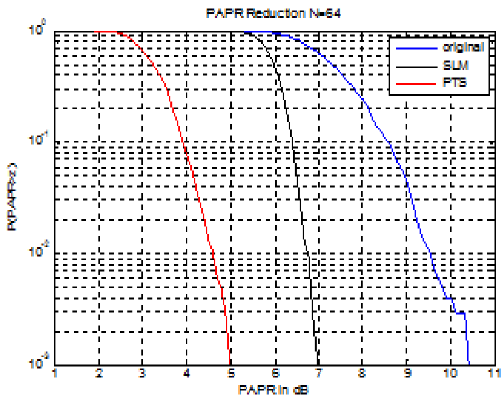

Figure 6. PAPR's CCDF using PTS method with N=64 and V=4 **Figure 7. PAPR's CCDF using SLM and PTS method with N=64**

Figure 6 shows that PTS technique improves the performance of OFDM system, moreover, it can be shown that with increasing the value of V the PAPR performance becomes better.

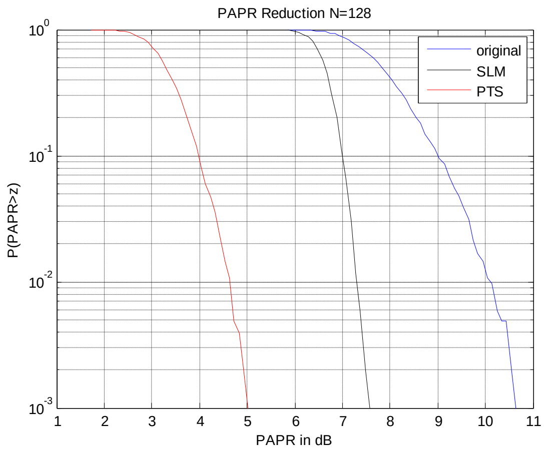

Figure 8. PAPR's CCDF using SLM and PTS method with N=128

In Figure 7 and Figure 8 it is clear that PTS method provides a better PAPR reduction performance compared to SLM method.

VI. CONCLUSIONS

OFDM is a very attractive technique for wireless communications due to its spectrum efficiency and channel robustness. One of the serious drawbacks of OFDM systems is that the composite transmit signal can exhibit a very high PAPR when the input sequences are highly correlated. In this paper, several important aspects are described as well as mathematical analysis is provided, including the distribution of the PAPR used in OFDM systems. Two typical signal scrambling techniques, SLM and PTS are investigated to reduce PAPR, all of which have the potential to provide substantial reduction in PAPR. PTS method performs better than SLM method in reducing PAPR.

REFERENCES

[1] Y.Wu and W. Y. Zou, “Orthogonal frequency division multiplexing: A multi-carrier modulation scheme,” IEEE Trans. Consumer Electronics, vol. 41, no. 3, pp. 392–399, Aug. 1995.

[2] University of Alberta, “Home page - High capacity digital communications laboratory,” 2007. Available: http://www.ece.ualberta.ca/~HCDC/mimohistory.html.

[3] Shinsuke Hara, Ramjee, “Principle and history of MCM/OFDM,” in Multicarrier techniques for 4G mobile communication, Artech House.

[4] E. Telatar, “Capacity of multi-antenna Gaussian channels,” European Transactions on Telecommunications, vol. 10, no 3, Dec 1999.

[5] Foschini G J, Gans M J, “On limits of wireless communication in a fading environment when using multiple antennas,” Wireless Personal Communication, vol. 6.

[6] KUANG Yu-jun, TENG Yong, “A new symbol synchronization scheme for cyclic prefix based systems,” The Journal of China Universities of Posts and Telecommunications.

[7] Peled A, Ruiz A, “Frequency domain data transmission using reduced computational complexity algorithms,” Acoustics, Speech, and Signal Processing, IEEE International Conference.

[8] Cooper, G.R, Nettleton, R.W, “A spread spectrum technique for high capacity mobile communications,” IEEE Transaction on Vehicular Technology, Nov 1978, vol. 27.

[9] H. Sampath, et al., “A fouth-generation MIMO-OFDM broadband wireless system: design, performance and field trial results,” IEEE Communication Magazine, Sep 2002, vol. 40, no 9.

[10] Jayalath, A.D.S, Tellainbura, C, “Side Information in PAR Reduced PTS-OFDM Signals,” Proceedings 14th IEEE Conference on Personal, Indoor and Mobile Radio Communications, Sept. 2003, vol.1.

[11] Oh-Ju Kwon and Yeong-Ho Ha, “Multi-carrier PAP reduction method using sub-optimal PTS with threshold,” IEEE Transactions on Broadcasting, June. 2003, vol. 49.

[12] Mohinder Jankiraman, “Peak to average power ratio,” in Space-time codes and MIMO systems, Artech House, 2004.

[13] Tao Jiang, Yiyan Wu,”peak to average power ratio reduction in OFDM systems”, IEEE transactions on broadcasting, vol. 54, no. 2, June 2008.

[14] Dov Wulich, “Defination of efficient PAPR in OFDM” IEEE communications letters, vol. 9, no. 9,September 2005.

[15] M.Palanivelan, Dr. Sheila Anand, M.Gunasekaran, “Matrix based low Complexity PAPR Reduction in OFDM Systems”, IJECT Vo l. 2, Issue 2, June 2011.

[16] Reena Chackochan, Dr. Himanshu Soni, “Comparative Analysis of Distortive and Non-Distortive OFDM Techniques for PAPR Reduction in Systems”, Proc. of Int. Conf. on Advances in Electrical & Electronics 2011.

[17] Tao Jiang, Member IEEE, and Yiyan Wu, Fellow, IEEE, “An Overview: Peak-to-Average Power Ratio Reduction Techniques for OFDM Signals” VOL. 54, NO. 2, 2008